Cell Reports

Article

ApoE4 Impairs Neuron-Astrocyte Coupling of Fatty Acid Metabolism

Graphical Abstract

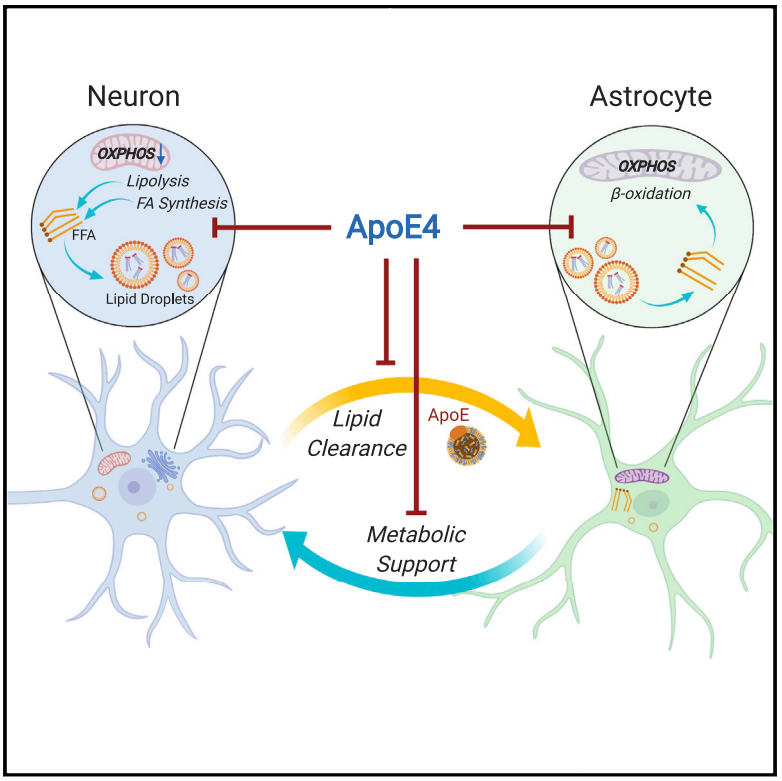

Highlights

- ApoE4 reduces the sequestering of FA in neuronal LD and elevates free FA levels
- FA in neuronal LD is transported to astrocyte in an ApoE isoform-dependent manner
- ApoE4 diminishes FA oxidation and elevates lipid content in astrocyte and in brain
- Astrocyte-to-neuron metabolic support depends on neuronal lipid clearance

Authors

Guoyuan Qi, Yashi Mi, Xiaojian Shi, Haiwei Gu, Roberta Diaz Brinton, Fei Yin

Correspondence

feiyin@arizona.edu

In Brief

Qi et al. reveal a role of Alzheimer's disease risk gene ApoE4 in disrupting fatty acid metabolism coupled between neuron and astrocyte. A systematic impairment in neuronal sequestering, neuron-to-astrocyte transport, and astrocytic degradation of fatty acids could contribute to lipid dysregulation, bioenergetic deficits, and increased Alzheimer's risk in ApoE4 carriers.

Qi et al., 2021, Cell Reports *34*, 108572
January 5, 2021
https://doi.org/10.1016/j.celrep.2020.108572

CellPress

Cell Reports

CellPress
OPEN ACCESS

Article

ApoE4 Impairs Neuron-Astrocyte Coupling of Fatty Acid Metabolism

Guoyuan Qi,[1,6] Yashi Mi,[1,6] Xiaojian Shi,[5] Haiwei Gu,[5] Roberta Diaz Brinton,[1,2,3,4] and Fei Yin[1,2,4,7,*]
[1]Center for Innovation in Brain Science, University of Arizona Health Sciences, Tucson, AZ 85724, USA
[2]Department of Pharmacology, College of Medicine Tucson, University of Arizona, Tucson, AZ 85724, USA
[3]Department of Neurology, College of Medicine Tucson, University of Arizona, Tucson, AZ 85724, USA
[4]Graduate Interdisciplinary Program in Neuroscience, University of Arizona, Tucson, AZ 85721, USA
[5]College of Health Solutions, Arizona State University, Scottsdale, AZ 85259, USA
[6]These authors contributed equally
[7]Lead Contact
*Correspondence: feiyin@arizona.edu
https://doi.org/10.1016/j.celrep.2020.108572

SUMMARY

Alzheimer's disease (AD) risk gene ApoE4 perturbs brain lipid homeostasis and energy transduction. However, the cell-type-specific mechanism of ApoE4 in modulating brain lipid metabolism is unclear. Here, we describe a detrimental role of ApoE4 in regulating fatty acid (FA) metabolism across neuron and astrocyte in tandem with their distinctive mitochondrial phenotypes. ApoE4 disrupts neuronal function by decreasing FA sequestering in lipid droplets (LDs). FAs in neuronal LDs are exported and internalized by astrocytes, with ApoE4 diminishing the transport efficiency. Further, ApoE4 lowers FA oxidation and leads to lipid accumulation in both astrocyte and the hippocampus. Importantly, diminished capacity of ApoE4 astrocytes in eliminating neuronal lipids and degrading FAs accounts for their compromised metabolic and synaptic support to neurons. Collectively, our findings reveal a mechanism of ApoE4 disruption to brain FA and bioenergetic homeostasis that could underlie the accelerated lipid dysregulation and energy deficits and increased AD risk for ApoE4 carriers.

INTRODUCTION

Apolipoprotein E (ApoE) is a lipid-binding protein that transports lipids across organs in the periphery and between different cell types in the brain (Hauser et al., 2011). Among its allelic variants in human, ε2, ε3, and ε4, the ε4 isoform (ApoE4) is the strongest genetic risk factor for the predominant, late-onset form of Alzheimer's disease (AD). Each ApoE4 allele increases AD risk by 3- to 4-fold while lowering the age at onset by ~8 years (Liu et al., 2013). Beyond its role in regulating amyloid-β (Aβ) aggregation and clearance—key processes underlying the prevailing hypothesis for AD etiology—ApoE4 is also associated with multiple neurological disorders including dementia with Lewy bodies, multiple sclerosis, and cerebrovascular disease (Belloy et al., 2019), suggesting an Aβ-independent mechanism in ApoE4 modification of disease risks.

Across ApoE4-affected neurological diseases, lipid dyshomeostasis is consistently manifested (Safieh et al., 2019). Lipids, including fatty acids (FAs), glycerolipids, phospholipids, and sterol lipids, constitute ~50% of brain dry weight (Hamilton et al., 2007). Because neurons have minimum capacity to catabolize FAs, and excessive FAs induce mitochondrial uncoupling and dysfunction, fine control and timely elimination of neuronal free FAs is critical to protect against neurodegeneration (Schönfeld and Reiser, 2017). A mechanism adapted by cells in peripheral organs to control lipotoxicity is to sequester free FAs as triacylglycerol (TAG) in intracellular lipid droplets (LDs) (Nguyen et al., 2017). These organelles store neutral lipids including TAG and sterol esters within a phospholipid monolayer and regenerate FAs for energetic needs upon starvation (Olzmann and Carvalho, 2019). In the brain, LDs accumulate in glial cells upon neuronal oxidative stress and during aging (Liu et al., 2015; Marschallinger et al., 2020), but whether and how LDs are involved in neuronal lipid metabolism remains poorly understood.

As the two most abundant, and energetically most essential cell types in the brain, neuron and astrocyte are coupled in not only glucose oxidation (Magistretti and Allaman, 2018; Yellen, 2018), but also lipid metabolism (Barber and Raben, 2019). Extensive studies have established the role of ApoE in mediating inter-cellular cholesterol transport from non-neuronal to neuronal cells (Björkhem et al., 1998; Mauch et al., 2001), with ApoE4-positive cells showing reduced function (Rawat et al., 2019; Yamazaki et al., 2019). Conversely, recent reports revealed a role of ApoE in transporting peroxidized FAs from neuron to astrocyte upon neuronal stimulation (Ioannou et al., 2019), and a substitution of fly glial apolipoprotein with human ApoE4 is associated with reduced glial LD accumulation (Liu et al., 2017), suggesting an isoform-dependent role of glial ApoE in internalizing extracellular FAs. However, because ApoE is also expressed in neurons under stress conditions (Xu

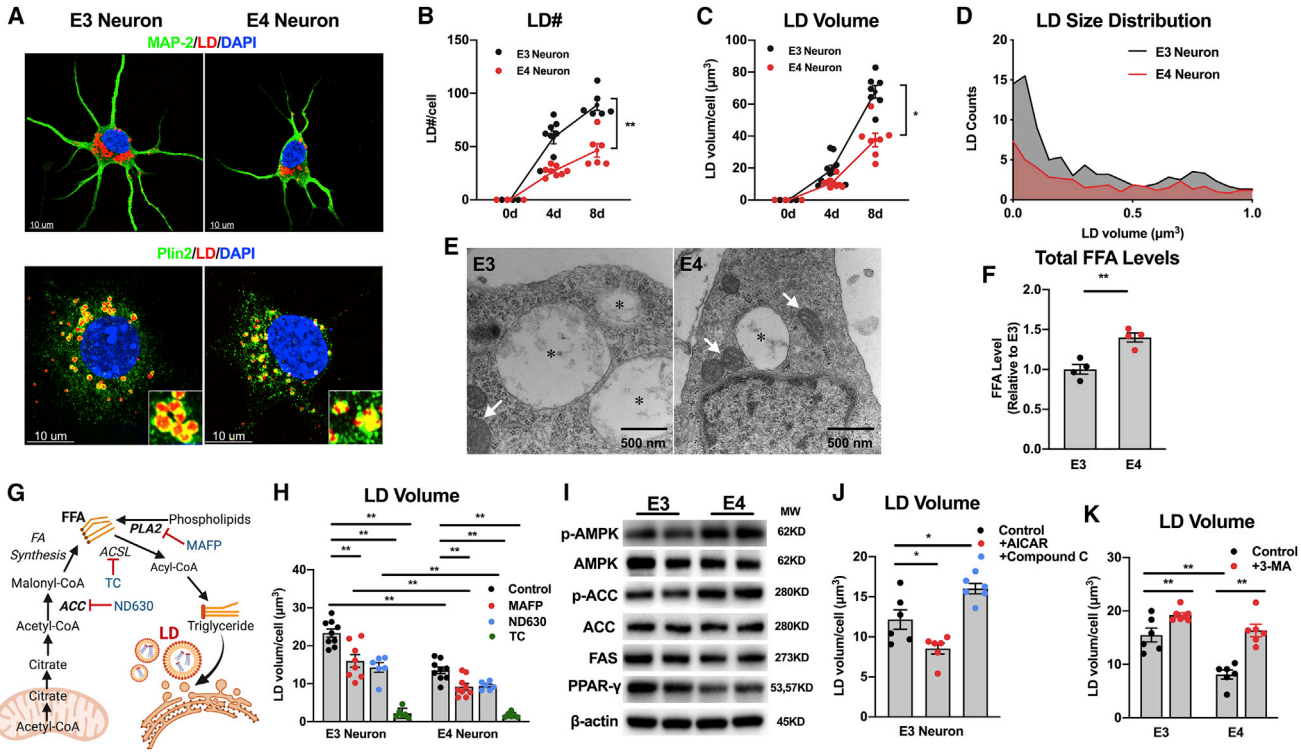

Figure 1. ApoE4 Decreases Neuronal Lipid Sequestering in Lipid Droplets

(A) Cropped images of DIV8 hippocampal neurons from ApoE3 and ApoE4 mice (E17) immunostained for LD, DAPI, and MAP-2 (upper panel) or Plin2 (lower panel).

(B and C) Number and volume of LDs per individual neuron on DIV0, DIV4, and DIV8.

(D) Distribution of LD sizes in DIV8 neurons binned between 0 and 1 μm^3.

(E) Representative TEM images of DIV8 neurons showing LDs (asterisk) and mitochondria (arrow).

(F) Total free FA levels in DIV8 neurons, n = 4.

(G) Schematic diagram of FA and LD metabolism-related pathways and inhibitors.

(H) LD volume in E3 and E4 neurons pretreated with MAFP, ND-630, TC, or vehicle for 12 h.

(I) Representative images showing protein levels of p-AMPK^{Thr172}, AMPK, p-ACC, ACC, SREBP-1c, FAS, and PPAR-γ in neurons (n = 4–6, quantified in Figure S1J).

(J) E3 neurons treated with AICAR, Compound C, or vehicle for 12 h were quantified for LD.

(K) E3 and E4 neurons treated with 3-MA or vehicle for 12 h were quantified for LD.

Data are presented as mean ± SEM. *p < 0.05, **p < 0.01. Data across all figures were from at least 3 animals or independent batches of cell cultures. For image-based quantifications in all figures, each data point represents the averaged value across all cells on a coverslip; n = 6–9 coverslips/condition, 8 ± 2 cells/coverslip. Scale bars, 10 μm (A); 500 nm (E). See also Figure S1.

et al., 2006), neurons cultured *in vitro* (Lin et al., 2018; Xu et al., 1999b), and neurons of selected brain regions *in vivo* (Han et al., 1994; Xu et al., 1999a), whether neuronal ApoE variants have an impact on inter-cellular FA metabolism, and whether astrocytic ApoE isoform alters the degradation of FAs, are unknown. Moreover, given that ApoE4 disrupts brain mitochondrial function via multiple mechanisms (Chen et al., 2011; Nuriel et al., 2017; Tambini et al., 2016; Zhao et al., 2017b) and mitochondria are involved in both the formation and degradation of LDs in non-CNS cells (Benador et al., 2019), the question also arises as to whether and how ApoE regulation of inter-cellular lipid metabolism is mechanistically connected with neuronal and astrocytic mitochondrial function.

Here, we report an isoform-dependent role of ApoE in regulating key mechanisms involved in neuron-astrocyte coupling of FA metabolism, from the sequestering of FAs by forming LDs in neurons, to the mobilization of neuronal LDs to FAs for transport to astrocytes, and eventually to the energetic degradation of FAs in astrocytes. In accordance with that, reduced FA oxidative capacity and elevated neutral lipid levels were manifested in ApoE4 mouse hippocampi.

RESULTS

ApoE4 Reduces Neuronal Lipid Sequestering in LD and Suppresses FA Synthesis

To determine how ApoE isoform affects lipid metabolism in neurons, primary embryonic neurons (E17) from the hippocampi of humanized ApoE3 (E3) and ApoE4 (E4) knockin mice were stained for neutral lipids. Strikingly, we observed substantial accumulation of LD-like lipid structures in neurons (Figure 1A; days *in vitro* 8 [DIV8]) under culture conditions without extra

NMDA stimulation or oxidative challenge used previously (Ioannou et al., 2019). We also confirmed that glutamate in culture medium did not alter LD accumulation (Figure S1A), and lipid peroxidation was not affected by ApoE genotype or glutamate levels (Figure S1B). These structures were located predominantly in the soma and surrounded by LD surface marker perilipin-2 (Plin2) (Figure 1A, lower panel). Both the counts and total volume (Figures 1B and 1C) of LDs increased with neuron maturing from DIV0 through DIV8 (Figures 1D and S1C–S1F). Exogenous FA (oleate-BSA) elevated neuronal LD accumulation (Figures S1G and S1H). Transmission electron microscopy (TEM) further visualized neuronal LDs as subcellular structures delimited by a single membrane leaflet, and most of them were adjacent to mitochondria (Figure 1E). We confirmed that neuronal LDs are not due to the introduction of humanized ApoE, because LDs in wild-type neurons were comparable to E3 neurons (Figure S1I). Intriguingly, compared to E3 neurons, E4 neurons accumulated fewer and smaller LDs (Figures 1B–1D) but higher FAs (Figure 1F). Because neurons have limited FA-degrading capacity via β-oxidation (Schönfeld and Reiser, 2017), increased FAs and reduced LDs suggested a lower ability of E4 neurons to store FA in LDs against lipid toxicity.

We next determined the mechanisms that contribute to neuronal LD formation and the lesser LDs in E4 neurons. Although short and medium-chain FAs are transported from the periphery, long- and very-long-chain FAs are primarily *de novo* synthesized in brain (Tracey et al., 2018) or generated by cytosolic phospholipase A2 (cPLA2)-catalyzed phospholipid hydrolysis (Du et al., 2009). To that end, E3 and E4 neurons were treated with inhibitors of acetyl-CoA carboxylase (ACC, rate-limiting enzyme of FA synthesis) or cPLA2 (Figure 1G). As long-chain FAs need to be activated by long-chain acyl-CoA synthetase (ACSL) before incorporation into LD, Triacsin C, an ACSL inhibitor (Igal et al., 1997) was used as a control for blocked LD formation (Figure 1G). ACC inhibition by ND-630 (Harriman et al., 2016) or cPLA2 by MAFP (Longo et al., 1999) for 24 h reduced LD volume in both E3 and E4 neurons (Figure 1H), indicating both *de novo* FA synthesis and lipolysis contributed to LD formation. Moreover, in the presence of ND-630 or MAFP, E4 neurons remained to show lower LD levels (Figure 1H), suggesting that their reduced LDs can be ascribed to both lowered lipolysis and FA synthesis. Key components of FA synthesis were downregulated in E4 neurons, as suggested by the higher inhibitory phosphorylation of ACC at Ser79 (+27.8%), and reduced expression of FA synthase (FAS, −16.3%) and PPAR-γ (−20.2%) (Figures 1I and S1J). AMP-activated protein kinase (AMPK), an inhibitory regulator of lipogenesis by phosphorylating ACC at Ser79 (Ha et al., 1994), was activated (p-AMPK^{Thr172}) in E4 neurons (Figures 1I and S1J). The regulatory role of AMPK in neuronal LD formation was further confirmed that its activator 5-aminoimidazole-4-carboxamide-1-b-D-ribofuranoside (AICAR) diminished, while its inhibitor compound C promoted, LD formation (Figure 1J).

In non-neuronal cells, autophagy can either promote LD formation by supplying recycled FAs or mediate LD mobilization via lipophagy (Singh et al., 2009; Zechner et al., 2005). Alternatively, LD can be mobilized by adipose triglyceride lipase (ATGL) (Smirnova et al., 2006). Our results indicated that inhibition of autophagy by 3-methyladenine (3-MA) led to LD accumulation in neurons (Figure 1K), whereas ATGL inhibitor atglistatin had no effect (Figure S1K), suggesting lipophagy as the major mechanism mediating constitutive LD turnover in neurons.

Impaired Bioenergetic Function and Neurite Outgrowth in ApoE4 Neurons

Because excessive FAs are known to inhibit mitochondrial function, we investigated the effect of ApoE4 on regulating neuronal bioenergetic function and its connection with FA metabolism. After confirming lower ApoE protein in E4 neurons (−35.9%) (Figures 2A and S2A), we evaluated ApoE isoform effect on OXPHOS and glucose metabolism. Compared to E3 controls, E4 neurons exhibited lower maximal respiration (respiration after mitochondrial uncoupling) (Figure S2B) and spare respiratory capacity ratio (SCR, the ratio of maximal to basal respiration, an indicator for utilization of OXPHOS capacity) but indistinguishable basal respiration (Figures 2B and 2C), which were accompanied by lower mitochondrial membrane potential ($\Delta\psi_m$) (Figure 2D) and cellular ATPs (Figure 2E). Reduced ATP levels were consistent with AMPK activation (Figure 1I). These bioenergetic outcomes in E4 neurons are likely accounted for by reduced expression of complex subunits (Figures 2F and S2C) and mitochondrial biogenesis regulators PGC1α (−23.6%) and PGC1β (−25.7%) (Figures 2G and S2D). In addition, TEM imaging revealed that mitochondria in E4 neurons are smaller and more dispersed in the cytoplasm (Figure 2H). Further, our data revealed that mitochondrial function is sensitive to compromised FA sequestering. When LD formation was blocked by ACSL inhibition, mitochondrial OXPHOS was significantly reduced (Figures 2I and 2J).

Glucose metabolism was also impaired in ApoE4 neurons as suggested by reduced glucose uptake (Figure 2K) and a decline in OXPHOS when glucose was the only fuel substrate (no pyruvate that bypasses glycolysis) (Figure 2L).

As a key metric of neuronal function, the outgrowth of neurites is energy-dependent and lipid-supported. Consistent with reports that ApoE4 decreases spine density and delays spine formation (Dumanis et al., 2009; Nwabuisi-Heath et al., 2014), the length, branch counts, and area of neurites were significantly lower in E4 versus E3 neurons (Figures 2M and 2N), which were in parallel with reduced levels of postsynaptic marker PSD-95 (−38.8%) and presynaptic marker SNAP-25 (−20.3%) (Figures 2O and S2E). Collectively, these findings suggest that ApoE4 in neurons dampened mitochondrial OXPHOS, glucose metabolism, neurite growth, and synaptic density, which were coupled with lower cellular levels of ApoE and impaired FA sequestering in LD.

ApoE4 Astrocytes Are Less Efficient in Mobilizing Neuronal LDs and Reducing FA Levels

Although oxidized free FAs can be transferred to astrocytes, whether neuronal LDs can be removed by astrocytes, and whether ApoE isoform affects this process, are unknown. We thus co-cultured DIV0 neurons with astrocytes of different genotype in a Transwell system, which enables content exchange but not physical contact (Figure 3A). Either E3 or E4 astrocytes dramatically reduced the number and volume of LDs in E3 or E4 neurons at DIV8, and E4 astrocytes showed a reduced ability to eliminate neuronal LDs (Figures 3B–3D). We then determined

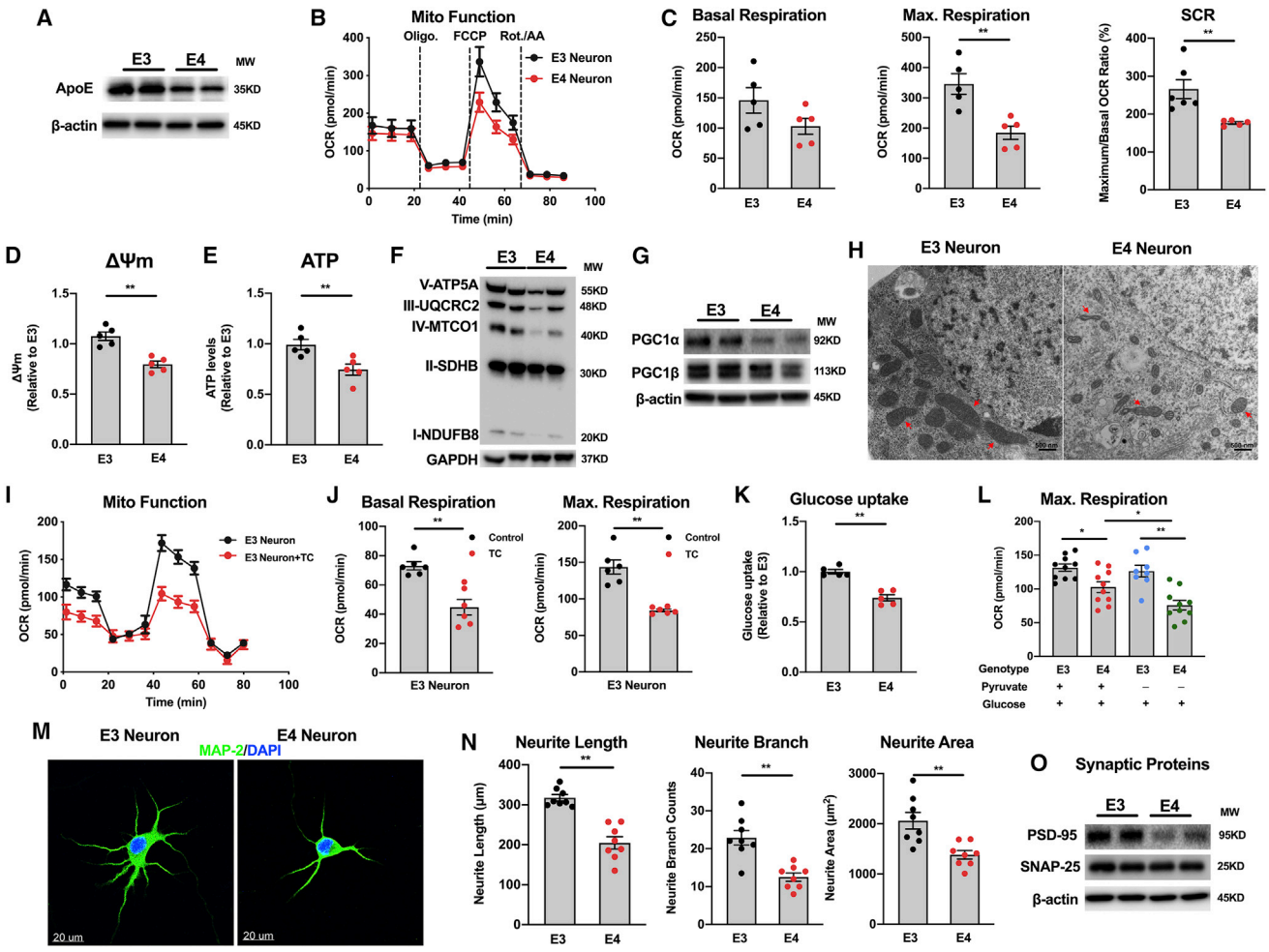

Figure 2. ApoE4 Neurons Exhibit Impaired Bioenergetic Function and Neurite Outgrowth

(A) Protein levels of ApoE in DIV8 E3 and E4 neurons (quantified in Figure S2A).

(B and C) Mitochondrial stress test performed on E3 and E4 neurons with sequential injections of mitochondrial inhibitors including oligomycin A, FCCP, and rotenone+antimycin A; basal and maximal respiration and spare capacity ratio (SCR) were determined.

(D) Mitochondrial membrane potential in neurons (n = 5).

(E) ATP levels in neurons (n = 5).

(F and G) Representative images for protein levels of mitochondrial complexes I–V subunits and PGC-1α and PGC-1β in neurons (quantified in Figures S2C and S2D).

(H) Representative TEM images of mitochondria (arrows) in neurons.

(I and J) Mitochondrial stress test performed on E3 neurons ± TC for 12 h; basal respiration and maximal respiration are shown.

(K) Glucose uptake capacity of E3 and E4 neurons.

(L) Mitochondrial stress test in E3 and E4 neurons supplied with glucose alone (25 mM) or glucose (25 mM) + pyruvate (1 mM); maximal respiration capacity is shown.

(M) Confocal images of neurons immunostained for MAP2.

(N) Length, branch count, and area of neurites in neurons; n = 8 coverslips/condition, 8 ± 2 cells/coverslip.

(O) Representative images of PSD-95 and SNAP-25 protein expression in neurons (quantified in Figure S2E).

Data are presented as mean ± SEM. *p < 0.05, **p < 0.01. For Seahorse assays across all figures, data shown are representative results of 3 independent experiments. Scale bars, 500 nm (H); 20 μm (M). See also Figure S2.

whether lowered neuronal LDs was due to reduced formation or increased clearance. Existing LDs in DIV8 E3 or E4 neurons were significantly reduced after E3 astrocyte exposure for 48 h (Figures 3E, 3F, and S3A), suggesting that astrocytes promote neuronal LD mobilization. The ApoE-isoform effect of astrocytes on clearing neuronal LDs was observed for E3 neurons only (Figures 3E and 3F), likely due to the reduced LD load in E4 neurons that made the ApoE-isoform effect in astrocytes less significant. Notably, LDs in E3 neurons were more efficiently cleared than those in E4 neurons after co-culturing with E3 astrocyte (Figures 3C–3E), suggesting that neuronal E4 may also impair LD mobilization and/or export.

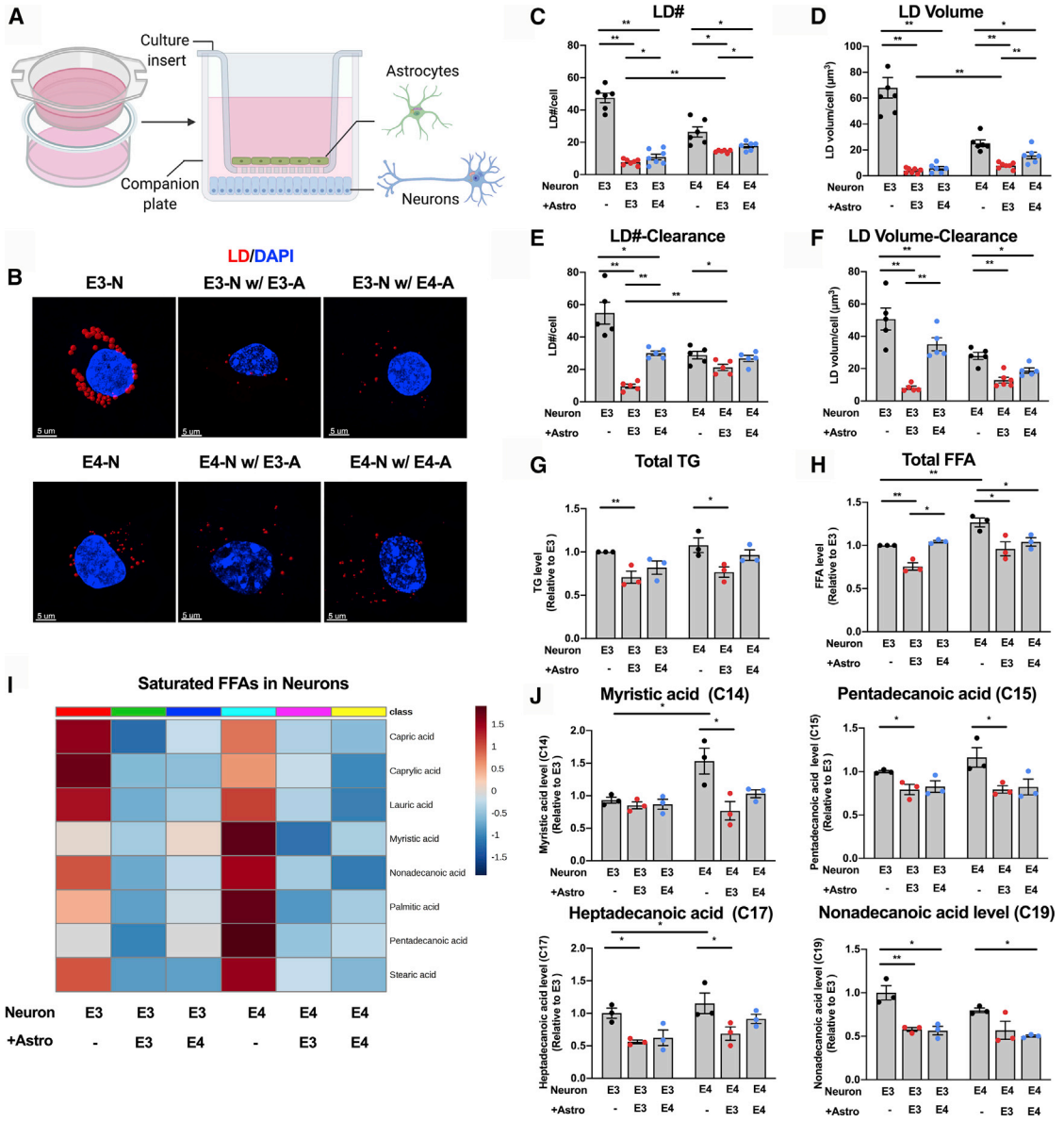

Figure 3. ApoE4 Astrocytes Are Less Capable to Clear Neuronal Lipid Droplets

(A) Schematic diagram of neuron-astrocyte co-culture system.

(B–D) LD in DIV0 E3 and E4 neurons cultured alone or co-cultured with either E3 or E4 astrocytes for 8 days.

(E and F) LD in DIV8 neurons cultured alone or co-cultured with astrocytes for 48 h.

(G and H) Total levels of triacylglycerol (TAG) and FAs in neurons cultured alone or co-cultured with astrocytes for 8 days.

(I) Heatmap of a panel of saturated, medium to long-chain free FAs in neurons cultured alone or co-cultured with astrocytes (n = 3).

(J) Levels of myristic acid (C14), pentadecanoic acid (C15), heptadecanoic acid (C17), and non-adecanoic acid (C19) in neurons following co-culture by targeted metabolomics.

Data are presented as mean ± SEM. *p < 0.05, **p < 0.01. For image-based quantifications, n = 5–7 coverslips/condition, 8 ± 2 cells/coverslip. Scale bars, 5 μm (B). See also Figure S3.

Consistent with reduced LD load, E3 astrocytes also reduced neuronal levels of TAG (Figure 3G) and FAs (Figure 3H). Targeted metabolomic analysis confirmed that neuronal levels of saturated, medium- to long-chain FAs (C8–C19) were reduced by astrocyte (Figure 3I), with pentadecanoic acid (C15) and heptadecanoic acid (C17) reaching statistical significance upon E3 astrocyte co-culture (Figure 3J). Similar reductions in unsaturated FAs were observed in neurons following co-culture (Figure S3B). Interestingly, despite lower LD levels (Figures 1A–1C), TAG in E4 neurons does not differ from that of E3 neurons (Figure 3G) that suggests reduced storage of free TAGs in LDs of E4 neurons. Together, these results support the role of

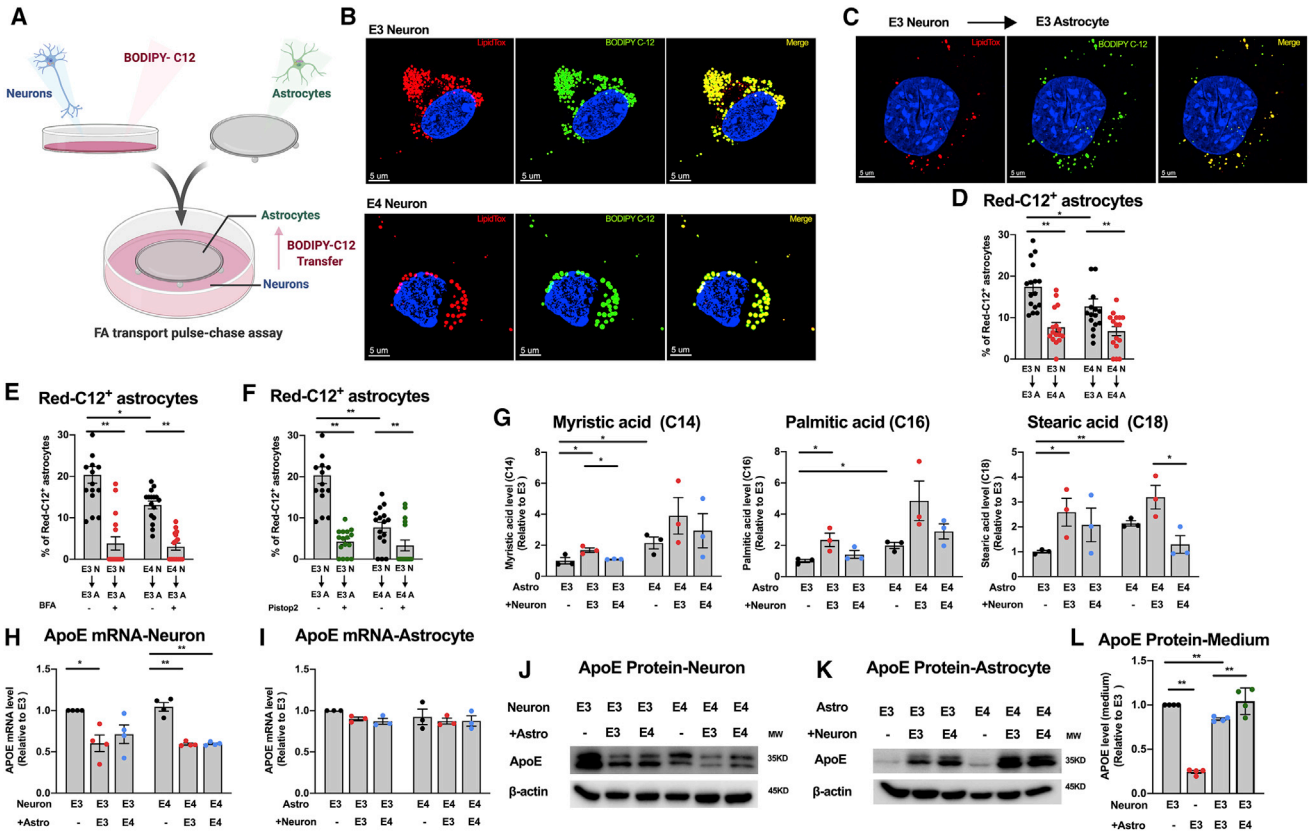

Figure 4. Transfer of FA from Neuron to Astrocyte Is Compromised by ApoE4

(A) Schematic diagram of neuron-astrocyte pulse-chase assay to trace FA trafficking in (B)–(F).

(B) Cropped images of neurons incubated with BODIPY-C12 for 16 h followed by co-staining for LD.

(C) Cropped images of E3 astrocytes co-cultured with BODIPY-C12-labeled E3 neurons for 4 h and co-stained for LD.

(D) Percentage of BODIPY-C12 positive cells in E3 or E4 astrocytes co-cultured with labeled E3 or E4 neurons for 4 h.

(E) Percentage of BODIPY-C12 positive cells in E3 astrocytes co-cultured with labeled E3 or E4 neurons with or without pre-treatment of BFA.

(F) Percentage of BODIPY-C12 positive cells in E3 or E4 astrocytes co-cultured with labeled E3 neurons with or without pre-treatment of Pistop2.

(G) Levels of myristic acid (C14), palmitic acid (C16), and stearic acid (C18) in astrocytes cultured alone or with neurons (n = 3).

(H–K) mRNA and protein levels of ApoE in astrocytes and neurons after co-culture for 8 days (n = 3–4, quantified in Figures S3G and S3H).

(L) ApoE levels in the medium of individual or co-culture systems (n = 4).

Data are presented as mean ± SEM. *p < 0.05, **p < 0.01. For pulse-chase assays, n = 4 coverslips/condition, 4 images/coverslip. Scale bars, 5 μm (B and C). See also Figure S3.

astrocyte in eliminating neuronal LDs and reveal the reduced capacity of E4 astrocytes in clearing neuronal lipids.

FAs in Neuronal LDs Are Transported to Astrocytes in an ApoE Isoform-Dependent Manner

It was revealed that human ApoE4 substitution of fly glial apolipoprotein reduced glial LD accumulation (Liu et al., 2017). We thus determined whether FAs in neuronal LDs are transported inter-cellularly to astrocytes, and if so, whether this process is modified by ApoE isoforms in neuron and astrocyte, as FA donor and recipient, respectively. Pulse-chase assay and a fluorescent FA analog BODIPY-C12 were used to track FA transfer (Figure 4A). After incubation, BODIPY-C12 were localized to neuronal LDs (Figure 4B); subsequent co-culture of these labeled neurons with astrocytes tracked BODIPY-C12 to astrocytes and localized to their LDs in 4 h (Figure 4C). Astrocyte-to-neuron transport of FAs was not observed in a reversed assay (Figure S3C). Importantly, neuron-to-astrocyte lipid transport was altered by ApoE4 in both cell types (Figure 4D and S3D): E4 astrocytes exhibited lower BODIPY-C12 positive rate than E3 astrocytes when co-cultured with E3 neurons, whereas E3 astrocytes received less lipids from E4 neurons than from E3 neurons (Figure 4D).

Because ApoE was found to facilitate neuronal FA transport to astrocytes, we determined whether previously identified secretory pathway in neuron and endocytosis pathway in astrocyte (Ioannou et al., 2019) were altered by ApoE isoforms. Our analyses suggested that disruption to Golgi secretory pathway by brefeldin A (BFA) (Figure 4E) or to endocytosis by Pitstop 2 (Figure 4F) substantially reduced FA transfer. Because LDL receptors are involved in neuron-to-astrocyte FA transfer (Ioannou et al., 2019), the lower ability of E4 astrocytes in uptaking LDL

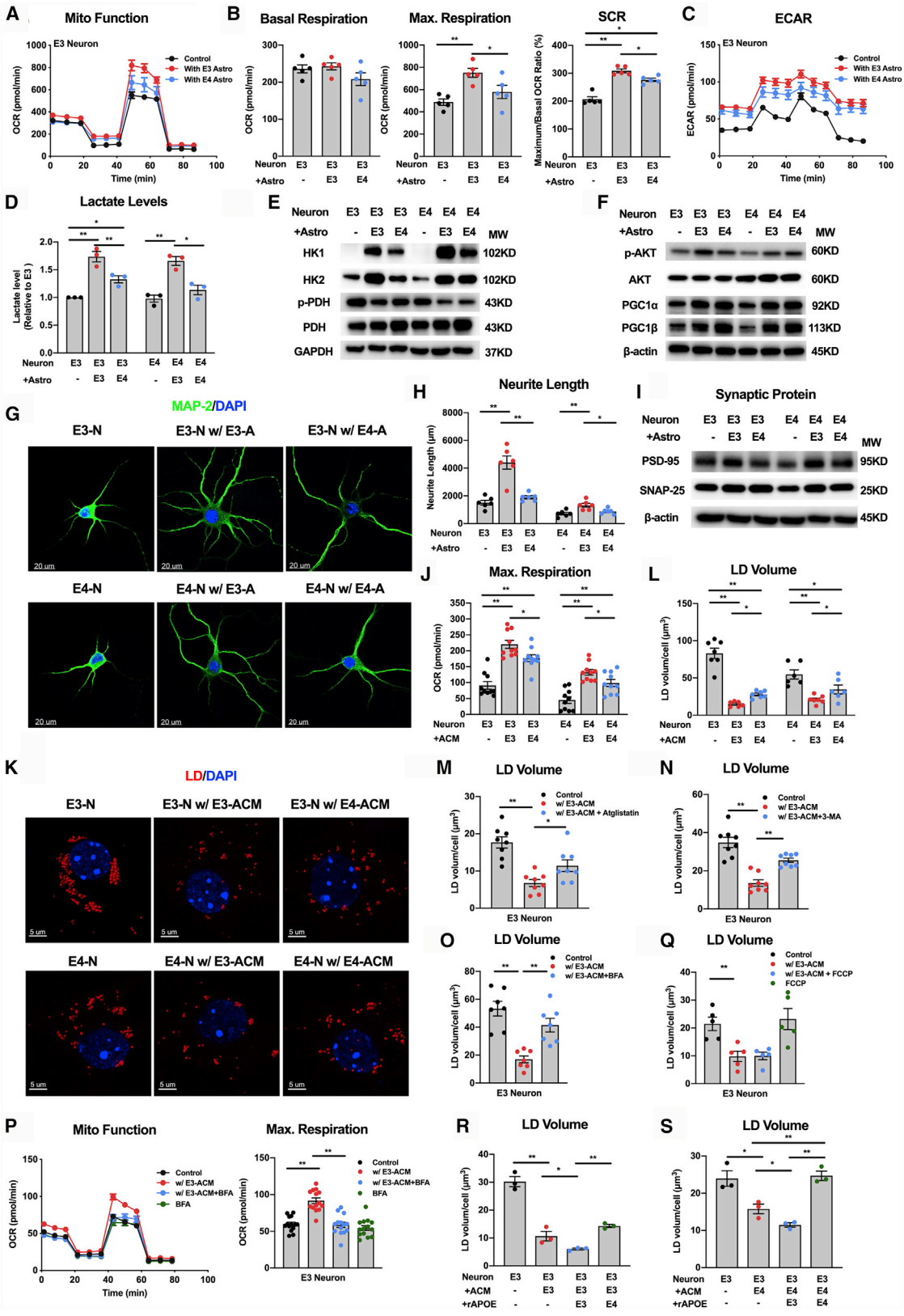

(legend on next page)

(Figure S3E) is consistent with a reduced capacity of E4 astrocytes in internalizing FAs. Moreover, saturated FAs including myristic acid (C14), palmitic acid (C16), and stearic acid (C18) were increased in E3 astrocytes after exposure to E3 neurons (Figures 4G and S3F). Interestingly, despite a reduced uptake ability, E4 astrocytes showed higher FA levels than E3 controls with or without neuronal co-culture (Figures 4G and S3F), indicating a disruption to FA degradation in E4 astrocytes.

Given the essential role of ApoE in mediating inter-cellular FA transfer (Ioannou et al., 2019; Liu et al., 2017), we investigated ApoE exchange between neuron and astrocyte. Astrocyte exposure significantly downregulated both mRNA (Figure 4H) and protein (Figures 4J and S3G) levels of ApoE in E3 or E4 neurons. The reduction in neuronal ApoE mRNA also suggests that the neurotrophic support by astrocytes may reduce neuronal ApoE expression by alleviating cellular stress (Xu et al., 2006). Simultaneously, ApoE protein was increased in astrocytes after co-culture (Figures 4K and S3H) with mRNA levels remained unchanged (Figure 4I), suggesting that elevated astrocytic ApoE could be transported from neurons together with FAs. Consistently, ApoE levels in the shared medium of E3-neuron-E3-astrocyte co-culture were lower than that of E3 neurons alone and higher than E3 astrocytes alone; however, E4 astrocytes were not able to alter ApoE in E3 neuron medium (Figure 4L). To further confirm the directionality of neuron-astrocyte exchange of ApoE, an ApoE4-specific antibody was used. As shown in Figure S3I, ApoE4 was not in E3 neurons co-cultured with E4 astrocytes but was detected in E3 astrocytes co-cultured with E4 neurons (Figure S3J). These data further support an ApoE-mediated unidirectional FA transport from neuron to astrocyte. Notably, no ApoE isoform effect was seen in reducing neuronal ApoE or elevating astrocytic ApoE (Figures 4H–4K), suggesting that the isoform effect on FAs transport could be primarily due to the differential lipid-carrying capacity (Yamazaki et al., 2019). These data collectively support a critical, isoform-dependent role of ApoE in mediating transport of neuronal lipids to astrocytes.

ApoE4 Astrocytes Exhibit Diminished Metabolic and Synaptic Support to Neurons

Astrocytes provide critical support to neurons for synapse formation/pruning, neurotransmitter modulation, and metabolic homeostasis (Bélanger et al., 2011; Jha and Morrison, 2018). We thus determined how ApoE variation in astrocyte regulates neuronal metabolic function and whether neuron-astrocyte coupling of FA metabolism is one of the underlying mechanisms. Metabolically, both mitochondrial function and aerobic glycolysis in E3 neurons was elevated by E3 astrocytes, as evidenced by elevated respiration (Figures 5A and 5B), ECAR (Figure 5C), and lactate levels (Figure 5D). However, these metabolic responses were diminished upon E4 astrocyte exposure (Figures 5A–5D). Similar differences between E3 and E4 astrocytes were observed when co-cultured with E4 neurons (Figures S4A–S4C). Lactate levels in co-culture medium were not changed by astrocytes (Figure S4D). Hexokinases 1 and 2 (HK1/2) and pyruvate dehydrogenase (PDH) controls glycolysis and the entry of pyruvate to TCA cycle, respectively. Consistent with the metabolic data, astrocyte exposure upregulated HK1 and HK2 expression while it reduced the inhibitory phosphorylation of PDH (p^{Ser293}) in neurons, with E4 astrocytes less effective than E3 astrocytes (Figures 5E and S4E). In parallel, key regulators of glucose metabolism (phospho-Akt) and mitochondrial biogenesis (PGC1α/β) were upregulated by astrocytes, and an ApoE isoform effect in astrocytes was seen for Akt activation in E3 neurons (Figures 5F and S4F).

Along with reduced bioenergetic support, diminished synaptic support by E4 astrocytes was also observed. Although E3 astrocytes triggered increased length (Figures 5G and 5H), area (Figure S4G), and branch counts (Figure S4H) of neurite, effects were significantly lessened with E4 astrocytes. In parallel, PSD-95 and SNAP-25 levels were increased by astrocyte co-culture, but E4 astrocytes were less capable in upregulating PSD-95 in E3 neurons (Figures 5I and S4I). Because lipoproteins are reported to facilitate the axonal growth of sympathetic neurons (Posse De Chaves et al., 2000), ApoE4-suppressed lipoprotein shuttle between astrocyte and neuron may be involved in the compromised synaptic support.

Bioenergetic Support of Astrocyte-to-Neuron Is Dependent on Neuronal LD Clearance

We next sought to determine the mechanism underlying the differential ability of E3 and E4 astrocytes in metabolically and synaptically supporting neurons. We first tested whether metabolic

Figure 5. ApoE4 Astrocytes Are Less Capable in Supporting Metabolic and Synaptic Functions of Neurons

(A and B) Mitochondrial respiration of E3 neurons cultured alone or with E3 or E4 astrocytes for 8 days; quantifications are shown in (B).
(C) ECAR of E3 neurons cultured alone or co-cultured with astrocytes as in (A) and (B).
(D) Lactate levels in neurons cultured alone or with astrocytes (n = 3).
(E) Representative images for protein levels of HK1, HK2, p-PDH^{Ser293}, and PDH in neurons cultured alone or with astrocytes (quantified in Figure S4E).
(F) Representative images for protein levels of p-AKT, AKT, PGC-1α, and PGC-1β in neurons cultured alone or with astrocytes (quantified in Figure S4F).
(G and H) Cropped images of neurons cultured alone or with astrocytes and immunostained for MAP2 (G); neurite length is quantified in (H).
(I) Representative images for protein levels of PSD-95 and SNAP-25 in neurons cultured alone or with astrocytes (quantified in Figure S4I).
(J) Mitochondrial maximal respiration of DIV8 neurons cultured with or without different astrocyte conditional medium (ACM) for 48 h.
(K and L) Cropped images and quantification of LD volumes in DIV8 neurons cultured with or without ACM for 48 h.
(M–O) LD volume in E3 neurons treated with vehicle, E3 ACM, or E3 ACM+atglistatin (M), E3 ACM+3-MA (N), or E3 ACM+BFA (O) for 12 h.
(P) Mitochondrial maximal respiration in E3 neurons treated with E3 ACM, BFA, E3 ACM+BFA, or vehicle for 12 h.
(Q) LD volume in E3 neurons treated with E3 ACM, FCCP, E3 ACM+FCCP, or vehicle for 12 h.
(R) LD volume in E3 neurons treated with E3 ACM, E3 ACM+rApoE3, or E3 ACM+rApoE4 for 24 h.
(S) LD volume in ApoE3 neurons treated with E4 ACM, E4 ACM+rApoE3, or E4 ACM+rApoE4 for 24 h.
Data are presented as mean ± SEM. *$p < 0.05$, **$p < 0.01$. For image-based quantifications, n = 3–8 coverslips/condition, 8 ± 2 cells/coverslip. Scale bars, 20 μm (G); 5 μm (K). See also Figure S4.

stimulation of neurons requires the physical presence of astrocytes that may serve as suppliers of fuels such as lactate and ketone bodies (Liu et al., 2017; Pellerin and Magistretti, 1994). Astrocyte-conditioned medium (ACM) of E3 or E4 astrocytes was found sufficient to upregulate neuronal mitochondrial respiration (Figures 5J, S4J, and S4K) and glycolysis (Figure S4L). Importantly, E3 ACM induced a greater rise in respiration and glycolysis than E4 ACM (Figures 5J and S4J–S4L). We reasoned that the distinctive capacity of E3 and E4 astrocytes in lipid clearance may be related to their ability in supporting neuronal function. Indeed, either E3 or E4 ACM was sufficient to reduce LD in neurons, with E3 ACM inducing a greater decline than E4 ACM (Figures 5K, 5L, and S4M). In contrast to neurons cultured alone (Figures 1K and S1K), both lipolysis and lipophagy contributed to ACM-induced mobilization of neuronal LDs as either atglistatin (Figure 5M) or 3-MA (Figure 5N) partially abolished LD clearance.

We next determined the mechanistic relationship between astrocyte regulation of neuronal OXPHOS and lipid removal. Intriguingly, blocking neuronal secretary pathway not only prevented ACM-induced LD removal (Figure 5O) but also abolished the increase in neuronal mitochondrial function (Figure 5P). Conversely, in the presence of OXPHOS uncoupler FCCP, ACM could still efficiently induce LD clearance (Figure 5Q). These results suggest that the ability of astrocyte to potentiate neuronal bioenergetic function is associated with, and dependent on, the removal of excessive neuronal lipids, whereas the mobilization of neuronal LDs by astrocyte does not rely on mitochondrial OXPHOS.

Excess ApoE3 Promotes, whereas Excess ApoE4 Inhibits, Astrocyte-Induced Neuronal LD Clearance

We next sought to determine whether ApoE4 disruption of neuron-astrocyte FA metabolic coupling is due to its reduced protein levels or its isoform. After supplementing neuron-ACM cultures with 10 nM recombinant ApoE3 (rApoE3) or ApoE4 (rApoE4) (Huang et al., 2017; Shi et al., 2017) for 24 h, neuronal LD clearance was determined. Interestingly, rApoE3 further reduced LDs in neurons cultured with E3-ACM (Figure 5R), indicating a positive effect of ApoE3 in clearing neuron LDs; in contrast, rApoE4 was unable to reduce neuronal LD. Similar results were obtained in neurons cultured with E4-ACM, where additional rApoE3 promoted LD clearance but rApoE4 completely abolished the effect elicited by E4-ACM (Figure 5S). Together, these data confirm the essential role of ApoE isoform in mediating neuronal lipid homeostasis and suggest ApoE3 as an enhancer of neuronal LD clearance and excessive ApoE4 as a negative regulator of the process.

ApoE4 Impairs Astrocytic FA Degradation and Leads to LD Accumulation

Astrocytes can efficiently synthesize and metabolize FAs. We therefore determined whether the differential ability of E3 and E4 astrocytes in clearing neuronal LDs was relevant to their capacity in storing and degrading lipids. Interestingly, when cultured alone, E4 astrocytes accumulated substantially more lipids in LDs than E3 astrocytes (Figures 6A–6C and S5A), which is consistent with previous findings in immortalized astrocytes (Farmer et al., 2019) and opposite to the effect of E4 in neurons (Figures 1A–1D). Nevertheless, as seen in neurons, saturated FAs including palmitic acid, myristic acid, and stearic acid were higher (Figure 4G), and ApoE proteins were lower (−41.0%) (Figure S5B), in E4 versus E3 astrocytes. We next assessed whether LD and FA accumulation in E4 astrocytes was due to increased lipogenesis or decreased FA degradation. The inhibition of *de novo* FA synthesis completely prevented LD accumulation in both E3 and E4 astrocytes (Figure 6D), suggesting that FA biosynthesis predominantly accounts for astrocytic LD formation. However, as the expression of key regulators of FA synthesis (SREBP1c, PPAR-γ, and FAS) in E4 astrocytes was either lower than, or indistinguishable from, E3 astrocytes (Figure S5C), we reasoned that elevated LDs in E4 astrocytes are likely attributed to reduced FA degradation. Indeed, E4 astrocytes exhibited reduced response in maximal respiration to exogenous FA palmitate-BSA (Figures 6E and 6F), suggesting their reduced capacity to perform β-oxidation. Consistently, when mitochondrial function was inhibited by FCCP, LDs in astrocytes increased substantially (Figures 6G and S5D), a response not observed in neurons (Figure 5Q). Further, metabolic flexibility assay using inhibitors of different fuel pathways including glucose, glutamine, and FA revealed that E4 astrocytes had a lower dependence and capacity of using FAs, whereas their ability to use glucose was higher than E3 astrocytes (Figure 6H).

The shift in the preference of E4 astrocytes toward glucose metabolism was further demonstrated by their higher basal respiration on glucose (Figures 6I and 6J), higher glycolytic rate (Figure 6K), and increased expression of multiple subunits of OXPHOS complexes (Figures 6L and S5E) and HK1 (Figures 6M and S5F). ATP levels were higher in E4 astrocytes (Figure 6N), which was consistent with a lower activation of AMPK (−31.8%) (Figures 6O and S5G). SCR, but not maximal respiration, was lower in E4 astrocytes (Figures S5H and S5I), largely due to the higher basal respiration (Figure 6J).

As fused mitochondria are more capable of performing FA β-oxidation (Rambold et al., 2015), we compared mitochondrial morphology in these astrocytes. Mitochondria in E4 astrocytes were more fragmented and formed less tubule structures compared to E3 controls (Figure 6P) as visualize in TEM imaging (Figure 6Q) and quantified by the ratio of fission-to-fusion products (Figure 6R). Consistently, an upregulation of mitochondrial fission regulator dynamin-related protein 1 (Drp1) (+42.7%), but not the fusion regulator optic atrophy 1 (OPA1), was observed in E4 astrocytes (Figures 6S and S5J). Together, these findings suggest that in astrocyte, E4-induced mitochondria fission is coupled with (1) a decline in degradation of FAs—either synthesized by astrocytes or transferred from neurons—that leads to FA and LD accumulation, and (2) a shift toward increased basal glucose metabolism that could be connected with their compromised metabolic support to neurons.

ApoE4 Induces a Metabolic Shift toward Diminished FA Metabolism and Enhanced Glucose Metabolism in Hippocampus

To determine whether ApoE4 disruption of FA metabolism occurs *in vivo*, we determined FA metabolizing capacity in brain slices and lipid content in brain tissues. Acute hippocampal

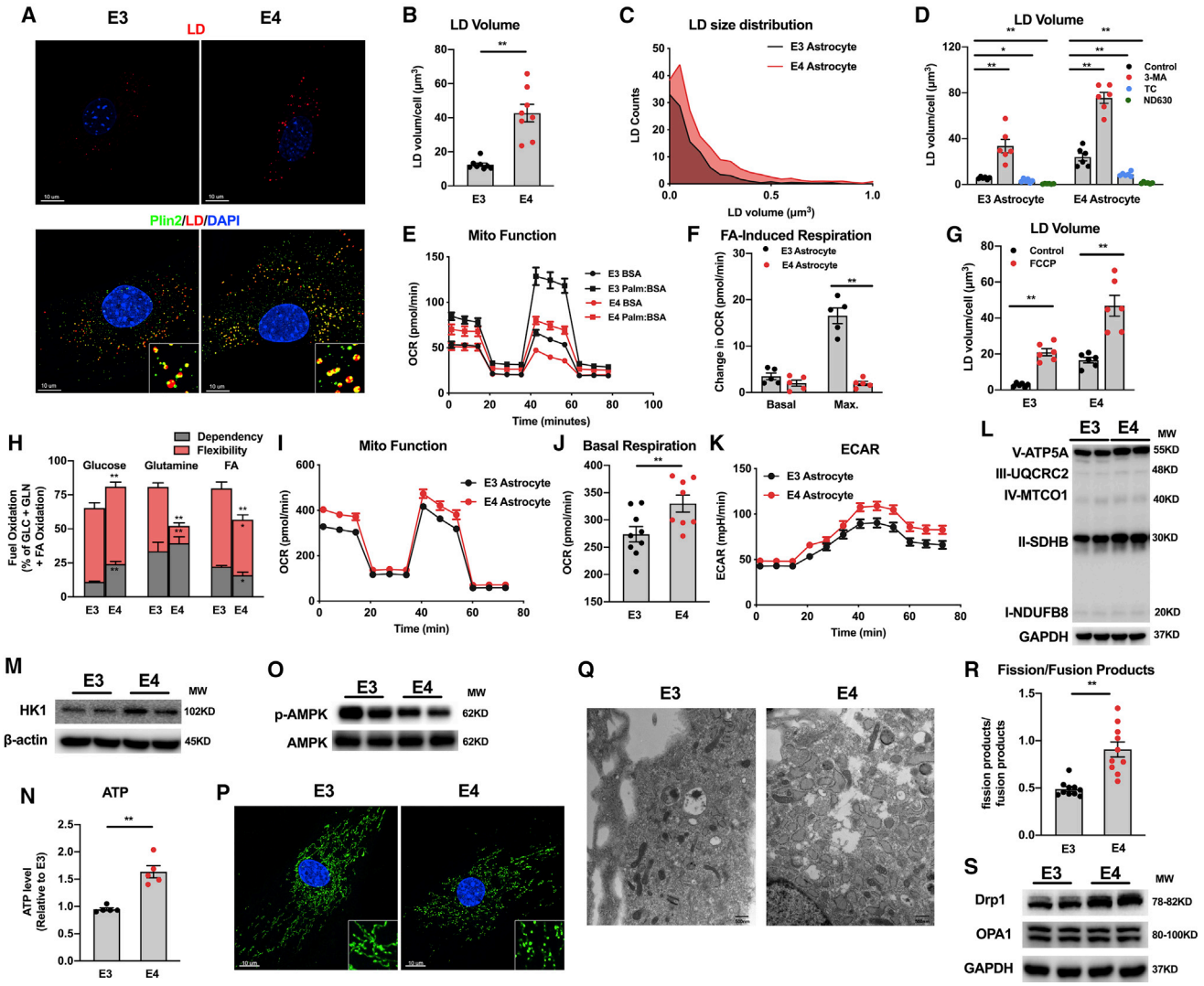

Figure 6. ApoE4 Alters Mitochondrial Phenotype, Suppresses Fatty Acid Degradation, and Accumulates Lipid Droplets in Astrocytes

(A) Cropped images of astrocytes isolated from E3 and E4 mice and immunostained for LD (upper panel) or co-stained for Plin2 (lower panel).

(B) LD volume in E3 or E4 astrocytes.

(C) Distribution of LD sizes in astrocytes binned between 0 and 1 μm^3.

(D) LD volume in astrocytes treated with 3-MA, TC, ND-630, or vehicle for 12 h.

(E and F) Exogenous FA-induced mitochondrial respiration in astrocytes was determined after supplying palmitoyl-BSA or BSA.

(G) LD volume in astrocytes treated with FCCP or vehicle for 12 h.

(H) Mitochondrial fuel flex test in astrocytes with the addition of inhibitors to glucose (mitochondrial pyruvate carrier inhibitor UK5099), glutamine (glutaminase inhibitor BPTES), and FA (CPT1 inhibitor etomoxir) pathways.

(I and J) Mitochondrial respiration in astrocytes with basal respiration shown in (J).

(K) ECAR in astrocytes.

(L and M) Representative images for expression of mitochondrial complex subunits and HK1 in astrocytes (quantified in Figures S5E and S5F).

(N) ATP levels in astrocytes.

(O) Representative images for p-AMPK^{Thr172} and AMPK levels in astrocytes (quantified in Figure S5G).

(P) Representative cropped confocal images of mitochondria reticulum in astrocytes.

(Q) Representative TEM images of mitochondrial structures in astrocytes.

(R) Ratio of fission products to fusion products in astrocytes by subtype analysis of mitochondria reticulum images.

(S) Representative images for protein expression of Drp1 and OPA1 in astrocytes (quantified in Figure S5J).

Data are presented as mean ± SEM. *$p < 0.05$, **$p < 0.01$. For image-based quantifications, n = 6–10 coverslips/condition, 8 ± 2 cells/coverslip. Scale bars, 10 μm (A and P); 500 nm (Q). See also Figure S5.

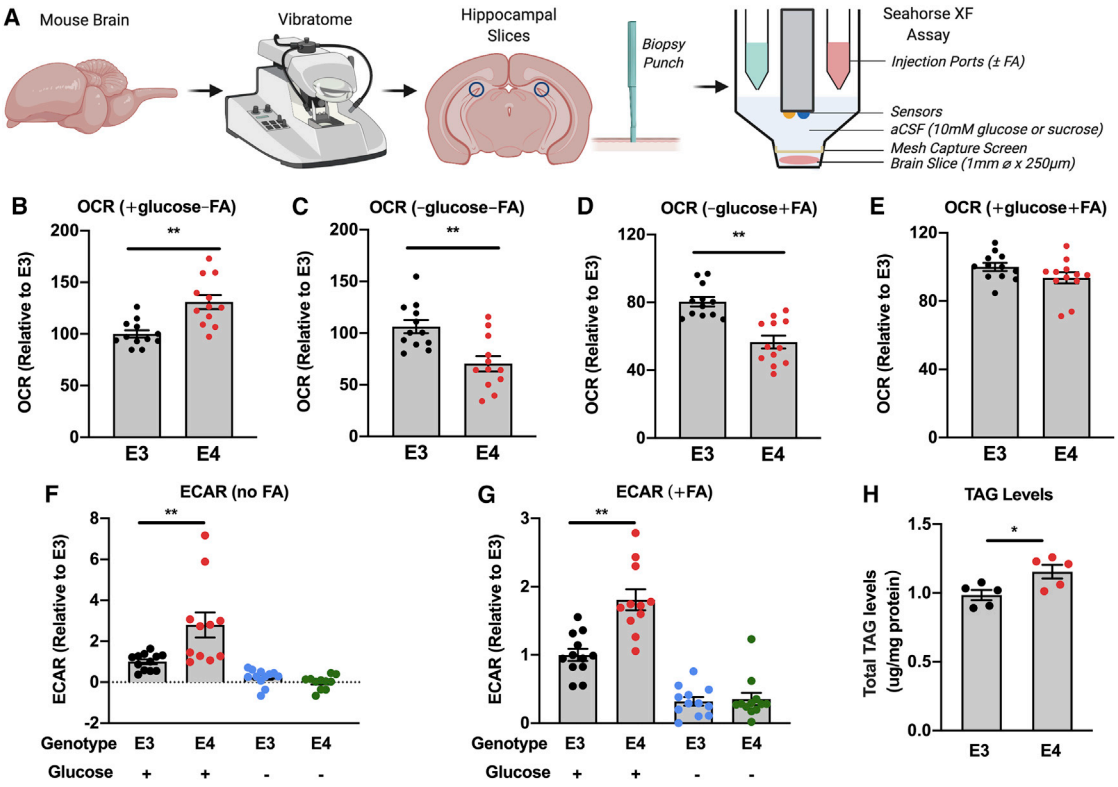

Figure 7. ApoE4 Diminishes FA Oxidation, Elevates Triacylglycerol Levels, and Promotes Glucose Metabolism in Mouse Hippocampus

(A) Schematic diagram to determine metabolic phenotype in acute hippocampal slices.

(B–E) Mitochondrial respiration of hippocampal slices with 10 mM glucose but no exogenous FA (B), no exogenous glucose or FA (C), 150 μM oleate-BSA but no glucose (D), or 10 mM glucose + 150 μM oleate-BSA (E).

(F and G) Acidification rate in hippocampal slices without (F) or with (G) exogenous FA (with 0 or 10 mM glucose).

(H) Total TAG levels in E3 and E4 mouse hippocampi.

Data are presented as mean ± SEM. *$p < 0.05$, **$p < 0.01$. (B–G) n = 12 slices from 3 animals; (H) n = 5 animals.

slices from E3 and E4 knockin mice were assessed for mitochondrial respiration and glycolysis with different fuel substrates (Figure 7A). E4 slices exhibited a higher basal respiration than E3 when glucose (10 mM), but not FA, was present (Figure 7B). However, upon glucose depletion, E4 slices showed an ~40% lower respiration than E3 (Figure 7C). These data suggest that E4 brains have higher glucose metabolism but a reduced ability to use non-glucose fuels. When exogenous FA (oleate-BSA) was supplemented, a lower respiration was seen in E4 slices, but only under aglycemic condition (Figure 7D), confirming a reduced β-oxidation in E4 brains. When both glucose and FA were present, the lack of significant differences (Figure 7E) suggests that the shift toward glucose metabolism in E4 brains is likely a compensation to FA metabolic deficit. In parallel with increased glucose respiration and decreased FA respiration, E4 brains showed a higher rate of aerobic glycolysis either with (Figure 7F) or without FA (Figure 7G). The minimum ECAR values under aglycemic conditions confirmed that the ApoE isoform effect under glycemic condition represented the variance in glycolytic rate. These *ex vivo* results validate our findings in astrocytes (Figures 6E–6K) and corroborate an impaired FA metabolism in E4 brains, which was further supported by higher TAG levels in the E4 hippocampi (Figure 7H). Together, these findings suggest that E4 brains could be more vulnerable to glucose hypometabolism because of their reduced capacity to use alternative fuels such as FAs. Despite the differences in FA metabolism and TAG levels *ex vivo* and *in vivo*, LD was not detectable in either strains at 3 months of age (result not shown). Given that ApoE4-implicated diseases are predominantly age-associated disorders, we speculate that brain accumulation of LDs *in vivo* likely requires advanced aging, metabolic stress, or pathological insults, which warrants future investigations.

DISCUSSION

Although FAs are important building blocks for membrane structures and substrates for energy reserve, high levels of FAs are connected with cellular toxicity and metabolic disorders. Control of FA levels is particularly critical for the brain because of its high energy demand and limited FA breakdown capacity. Catabolism of FA by β-oxidation and sequestering of FA in intracellular LDs are two complementary pathways used by peripheral organs to reduce intracellular FA burden and protect cells from lipotoxicity. Our findings suggest that in the brain, FA levels are

regulated in a cell-type-specific manner: FA biosynthesis and incorporation into LDs determine neuronal FA and LD levels, whereas for astrocytes, their capacity in degrading FAs appears to be more significant. Such cell-autonomous strategies against FA toxicity underlie the differential effect of ApoE variation on LD levels across cell types.

Our data indicate that in the absence of astrocytes, neurons sequester excess FAs as TAG in their own LDs. Compared to E3 neurons, E4 neurons exhibit reduced capability in forming LDs. Elevated FAs subsequently contribute to mitochondrial dysfunction and ATP deficiency in E4 neurons. We show that when FA sequestering to LD is blocked, mitochondrial function is decreased, and when neuronal FA export is inhibited, mitochondrial potentiation by ACM is also abolished. This is consistent with the detrimental effect of high levels of FAs or acyl-CoA on mitochondrial function (Li et al., 2010; Schönfeld and Reiser, 2017). In response to low ATP and high FA levels, AMPK is activated in E4 neurons, which suppresses *de novo* synthesis of FAs by phosphorylating and inhibiting ACC, likely as an adaptive response to alleviate FA toxicity. Hence, our data suggest that ApoE4-induced perturbation to FA homeostasis underlies its negative effect on neuronal bioenergetic and synaptic function, besides its direct effect on mitochondria via domain interactions (Chen et al., 2011).

Notably, lactate from glial cells is not the major substrate for neuronal LD synthesis in our model. First, both E3 and E4 neurons form LDs in the absence of astrocytes using FAs from *de novo* synthesis and lipolysis. Second, when astrocytes are present, lactate levels increase in neurons, but not in the co-culture medium, suggesting its neuronal origination instead of being transported from astrocytes. This is consistent with a recent report that astrocyte-derived lactate is not required for the bioenergetic response to stimulation in neurons (Díaz-García et al., 2017). Interestingly, while autophagy contributes to LD formation in NMDA-stimulated neurons (Ioannou et al., 2019), our results suggest that the autophagic mechanism primarily facilitates the mobilization of neuronal LDs via lipophagy.

In contrast to neurons, astrocytes can efficiently metabolize FAs. FA oxidation—predominantly in astrocytes—contributes ~20% of total brain energy supply (Ebert et al., 2003). Our data suggest that reduced FAs catabolism is the main process accounting for the elevation in FA and LD levels in E4 astrocytes. The lower capacity of E4 astrocytes in metabolizing FAs is consistent with the shift of mitochondrial dynamics toward fission products, which are less efficient in distributing and oxidizing FAs compared to fused, tubular mitochondria (Rambold et al., 2015).

In neuron-glia co-culture, mitochondrial OXPHOS inhibitor rotenone or the knockout of Ndufs4 in neurons leads to glial LD accumulation (Liu et al., 2015). Our findings suggest that the metabolic phenotype of astrocyte also modulates their LD load. E4 astrocytes, with decreased FA catabolizing capacity, exhibit increased LD levels, as seen in astrocytes with OXPHOS inhibition. These findings are in line with a previous report in *Drosophila* that loss of a mitochondrial FA importer leads to LD accumulation in the brain (Schulz et al., 2015). As such, we speculate that the accumulation of glial LDs in Ndufs4$^{-/-}$ mouse brain may also be related to the inefficiency of their glial cells in degrading FAs. Further investigations in mice with cell-type-specific mitochondrial dysfunction are needed to distinguish these two processes. Overall, our data support the critical role of astrocytic mitochondria in performing β-oxidation and thereby modulating brain lipid homeostasis.

The capacity in performing glycolysis and OXPHOS varies between neuron and astrocyte (Magistretti and Allaman, 2018; Yellen, 2018). Our findings suggest that ApoE4 elicits a decline in glucose-dependent OXPHOS in neurons but an increase in astrocytes. This is consistent with dysfunctional neurons and activated astrocytes seen in both ApoE4 mice (Zhu et al., 2012) and AD brains (Long and Holtzman, 2019). Notably, a recent proteomic network analysis of post-mortal brains revealed the activation of a module enriched for glucose metabolism and glial proteins in AD cases, with the ApoE4 homozygous sub-group most affected (Johnson et al., 2020).

Upon oxidative stress or hyperactivity, neurons transfer peroxidized FAs to glia via ApoE-positive lipid particles (Ioannou et al., 2019). We found that lipids in neuronal LDs can also be transferred to astrocytes, with E4 neurons and E4 astrocytes less efficient in exporting and internalizing FAs, respectively. Intriguingly, while ApoE transports cholesterol from astrocyte to neuron, the transfer of FAs is from neuron to astrocyte only. This suggests that the neuron-astrocyte coupling of FA metabolism is a highly regulated pathway activated by astrocyte-originated signals, although the messengers that initiate neuronal LD mobilization remain to be determined. In parallel with LD and FA transfer, ApoE protein levels decrease in neurons and increase in co-cultured astrocytes, supporting the transport of neuronal FAs in ApoE-mediated lipid particles.

It is noteworthy that higher ApoE protein levels in neurons cultured alone are likely relevant to the more stressed *in vitro* environment. This is supported by the decline in both ApoE mRNA and protein levels upon co-culture with the neurotrophic astrocytes. Interestingly, neurons were found to synthesize and secrete as much as 20% of brain ApoE under physiological conditions (Knoferle et al., 2014), and human studies also detected neuronal ApoE mRNA (Xu et al., 1999a) and protein (Han et al., 1994). Our study supports an essential role of neuronal ApoE that is particularly critical upon pathological conditions such as stress, injury, or lack of astrocyte neurotrophic support.

ApoE4 shows both loss-of-function and gain-of-toxic-function across various AD pathogenesis pathways (Yamazaki et al., 2019). Although our findings support the notion that ApoE4 disruption of neuron-astrocyte FA metabolism is primarily due to its isoform, supplemental ApoE3 protein exhibits beneficial effect on neuronal LD clearance. This isoform-dependent dose-response relationship suggests that a direct comparison of ApoE3 and ApoE4 protein levels could be complicated by their structural and functional distinctions. Nevertheless, it is notable that reduced ApoE protein in ApoE4 cells was found to originate from increased proteolytic degradation due to the special conformation of ApoE4 (Mahley and Huang, 2012). This is consistent with our results that ApoE4 isoform alters protein, but not mRNA levels of ApoE in both cell types.

Astrocytes are known to promote neuronal function via various mechanisms, including fuel and cholesterol supply, release of neurotrophic factors, and donation of mitochondria (Hayakawa

et al., 2016; Qi et al., 2020). Our results indicate that ApoE4 impairs the bioenergetic and synaptic support of astrocyte to neurons, and the enhancement of neuronal bioenergetics is dependent on the clearance of neuronal lipids, thus suggesting an unappreciated mechanistic connection between ApoE4 and neuronal mitochondrial dysfunction via inter-cellular coupling of lipid metabolism. Further, our study reveals that neuronal mitochondrial enhancement does not require continuous lactate supply from astrocytes as suggested by results from neuron-ACM co-cultures.

Lipid dyshomeostasis and accumulations of lipid particles have been increasingly investigated in aging and AD brains (Chan et al., 2012; Di Paolo and Kim, 2011; Hamilton et al., 2015; Marschallinger et al., 2020; Shimabukuro et al., 2016). In fact, among the top risk genes for sporadic AD, *APOE*, *TREM2*, *APOJ*, *PICALM*, *ABCA7*, and *SORL1* are all directly involved in lipid trafficking or metabolism (Karch and Goate, 2015). Our findings on the detrimental role of ApoE4 in mediating neuron-astrocyte coupling of lipid metabolism is consistent with the compromised function of ApoE4 astrocytes in cholesterol trafficking (Zhao et al., 2017a). These lines of evidence support a mechanistic role of lipid metabolism in AD etiology beyond amyloid and Tau pathologies. Given the central role of lipid species in synapse formation, Aβ clearance, white matter integrity, and neuroinflammation, targeting the disrupted intracellular lipid sequestering and inter-cellular lipid exchange might represent a potential therapeutic strategy against AD, especially for those who carry the ApoE4 allele(s).

STAR★METHODS

Detailed methods are provided in the online version of this paper and include the following:

- KEY RESOURCES TABLE
- RESOURCE AVAILABILITY
  - Lead Contact
  - Materials Availability
  - Data and Code Availability
- EXPERIMENTAL MODEL AND SUBJECT DETAILS
- METHOD DETAILS
  - Isolation and culture of primary hippocampal neurons
  - Isolation and culture of primary astrocytes
  - Co-culture of primary neurons with astrocytes
  - Neuronal culture with astrocyte conditioned medium (ACM)
  - Immunostaining and confocal imaging
  - Lipid droplets staining and quantification
  - RNA extraction and RT-qPCR
  - Cellular glucose uptake assay
  - Mitochondrial membrane potential
  - LDL uptake assay
  - Lipid peroxidation assay
  - ApoE levels in culture medium
  - Lactate levels
  - Total triacylglycerol
  - Total free fatty acids
  - Unsaturated fatty acids
  - ATP levels
  - Mitochondrial flux assay
  - Mitochondrial FA metabolic test
  - Mitochondrial fuel flex test
  - Acute brain slice metabolic analysis
  - Immunoblotting and quantification
  - Inter-cellular fatty acid transfer (pulse-chase) assay
  - Transmission electron microscope (TEM) analysis
  - Mitochondrial morphological subtype analysis
  - Fatty acid mass spectrometry (MS) analysis
- QUANTIFICATION AND STATISTICAL ANALYSIS

SUPPLEMENTAL INFORMATION

Supplemental Information can be found online at https://doi.org/10.1016/j.celrep.2020.108572.

ACKNOWLEDGMENTS

This work was supported by the University of Arizona Center for Innovation in Brain Science startup fund (to F.Y.), NIA (P01AG026572 to R.D.B.: Project 1 to R.D.B. and Analytic Core to F.Y.), and Arizona Alzheimer's Consortium Pilot Project (to F.Y.). Schematic illustrations were created with https://BioRender.com.

AUTHOR CONTRIBUTIONS

Conceptualization, F.Y.; Methodology, F.Y., G.Q., Y.M., and R.D.B.; Investigation, G.Q., Y.M., X.S., and H.G.; Formal Analysis, G.Q., Y.M., and F.Y.; Writing – Original Draft, F.Y., G.Q., and Y.M.; Writing – Review & Editing, F.Y., G.Q., Y.M., R.D.B., and H.G.; Funding Acquisition, F.Y. and R.D.B.

DECLARATION OF INTERESTS

The authors declare no competing interests.

Received: May 15, 2020
Revised: November 16, 2020
Accepted: December 8, 2020
Published: January 5, 2021

REFERENCES

Barber, C.N., and Raben, D.M. (2019). Lipid Metabolism Crosstalk in the Brain: Glia and Neurons. Front. Cell. Neurosci. *13*, 212.

Batiuk, M.Y., de Vin, F., Duqué, S.I., Li, C., Saito, T., Saido, T., Fiers, M., Belgard, T.G., and Holt, M.G. (2017). An immunoaffinity-based method for isolating ultrapure adult astrocytes based on ATP1B2 targeting by the ACSA-2 antibody. J. Biol. Chem. *292*, 8874–8891.

Bélanger, M., Allaman, I., and Magistretti, P.J. (2011). Brain energy metabolism: focus on astrocyte-neuron metabolic cooperation. Cell Metab. *14*, 724–738.

Belloy, M.E., Napolioni, V., and Greicius, M.D. (2019). A Quarter Century of APOE and Alzheimer's Disease: Progress to Date and the Path Forward. Neuron *101*, 820–838.

Benador, I.Y., Veliova, M., Liesa, M., and Shirihai, O.S. (2019). Mitochondria Bound to Lipid Droplets: Where Mitochondrial Dynamics Regulate Lipid Storage and Utilization. Cell Metab. *29*, 827–835.

Björkhem, I., Lütjohann, D., Diczfalusy, U., Ståhle, L., Ahlborg, G., and Wahren, J. (1998). Cholesterol homeostasis in human brain: turnover of 24S-hydroxycholesterol and evidence for a cerebral origin of most of this oxysterol in the circulation. J. Lipid Res. *39*, 1594–1600.

Chan, R.B., Oliveira, T.G., Cortes, E.P., Honig, L.S., Duff, K.E., Small, S.A., Wenk, M.R., Shui, G., and Di Paolo, G. (2012). Comparative lipidomic analysis

of mouse and human brain with Alzheimer disease. J. Biol. Chem. *287*, 2678–2688.

Chen, H.K., Ji, Z.S., Dodson, S.E., Miranda, R.D., Rosenblum, C.I., Reynolds, I.J., Freedman, S.B., Weisgraber, K.H., Huang, Y., and Mahley, R.W. (2011). Apolipoprotein E4 domain interaction mediates detrimental effects on mitochondria and is a potential therapeutic target for Alzheimer disease. J. Biol. Chem. *286*, 5215–5221.

Chong, J., Wishart, D.S., and Xia, J. (2019). Using MetaboAnalyst 4.0 for Comprehensive and Integrative Metabolomics Data Analysis. Curr. Protoc. Bioinformatics *68*, e86.

Di Paolo, G., and Kim, T.W. (2011). Linking lipids to Alzheimer's disease: cholesterol and beyond. Nat. Rev. Neurosci. *12*, 284–296.

Díaz-García, C.M., Mongeon, R., Lahmann, C., Koveal, D., Zucker, H., and Yellen, G. (2017). Neuronal Stimulation Triggers Neuronal Glycolysis and Not Lactate Uptake. Cell Metab. *26*, 361–374.e4.

Du, L., Hickey, R.W., Bayir, H., Watkins, S.C., Tyurin, V.A., Guo, F., Kochanek, P.M., Jenkins, L.W., Ren, J., Gibson, G., et al. (2009). Starving neurons show sex difference in autophagy. J. Biol. Chem. *284*, 2383–2396.

Dumanis, S.B., Tesoriero, J.A., Babus, L.W., Nguyen, M.T., Trotter, J.H., Ladu, M.J., Weeber, E.J., Turner, R.S., Xu, B., Rebeck, G.W., and Hoe, H.S. (2009). ApoE4 decreases spine density and dendritic complexity in cortical neurons in vivo. J. Neurosci. *29*, 15317–15322.

Ebert, D., Haller, R.G., and Walton, M.E. (2003). Energy contribution of octanoate to intact rat brain metabolism measured by 13C nuclear magnetic resonance spectroscopy. J. Neurosci. *23*, 5928–5935.

Farmer, B.C., Kluemper, J., and Johnson, L.A. (2019). Apolipoprotein E4 Alters Astrocyte Fatty Acid Metabolism and Lipid Droplet Formation. Cells *8*, 182.

Fried, N.T., Moffat, C., Seifert, E.L., and Oshinsky, M.L. (2014). Functional mitochondrial analysis in acute brain sections from adult rats reveals mitochondrial dysfunction in a rat model of migraine. Am. J. Physiol. Cell Physiol. *307*, C1017–C1030.

Gu, H., Zhang, P., Zhu, J., and Raftery, D. (2015). Globally Optimized Targeted Mass Spectrometry: Reliable Metabolomics Analysis with Broad Coverage. Anal. Chem. *87*, 12355–12362.

Ha, J., Daniel, S., Broyles, S.S., and Kim, K.H. (1994). Critical phosphorylation sites for acetyl-CoA carboxylase activity. J. Biol. Chem. *269*, 22162–22168.

Hamilton, J.A., Hillard, C.J., Spector, A.A., and Watkins, P.A. (2007). Brain uptake and utilization of fatty acids, lipids and lipoproteins: application to neurological disorders. J. Mol. Neurosci. *33*, 2–11.

Hamilton, L.K., Dufresne, M., Joppé, S.E., Petryszyn, S., Aumont, A., Calon, F., Barnabé-Heider, F., Furtos, A., Parent, M., Chaurand, P., and Fernandes, K.J. (2015). Aberrant Lipid Metabolism in the Forebrain Niche Suppresses Adult Neural Stem Cell Proliferation in an Animal Model of Alzheimer's Disease. Cell Stem Cell *17*, 397–411.

Han, S.H., Einstein, G., Weisgraber, K.H., Strittmatter, W.J., Saunders, A.M., Pericak-Vance, M., Roses, A.D., and Schmechel, D.E. (1994). Apolipoprotein E is localized to the cytoplasm of human cortical neurons: a light and electron microscopic study. J. Neuropathol. Exp. Neurol. *53*, 535–544.

Harriman, G., Greenwood, J., Bhat, S., Huang, X., Wang, R., Paul, D., Tong, L., Saha, A.K., Westlin, W.F., Kapeller, R., and Harwood, H.J., Jr. (2016). Acetyl-CoA carboxylase inhibition by ND-630 reduces hepatic steatosis, improves insulin sensitivity, and modulates dyslipidemia in rats. Proc. Natl. Acad. Sci. USA *113*, E1796–E1805.

Hauser, P.S., Narayanaswami, V., and Ryan, R.O. (2011). Apolipoprotein E: from lipid transport to neurobiology. Prog. Lipid Res. *50*, 62–74.

Hayakawa, K., Esposito, E., Wang, X., Terasaki, Y., Liu, Y., Xing, C., Ji, X., and Lo, E.H. (2016). Transfer of mitochondria from astrocytes to neurons after stroke. Nature *535*, 551–555.

Huang, Y.A., Zhou, B., Wernig, M., and Südhof, T.C. (2017). ApoE2, ApoE3, and ApoE4 Differentially Stimulate APP Transcription and Aβ Secretion. Cell *168*, 427–441.e21.

Igal, R.A., Wang, P., and Coleman, R.A. (1997). Triacsin C blocks de novo synthesis of glycerolipids and cholesterol esters but not recycling of fatty acid into phospholipid: evidence for functionally separate pools of acyl-CoA. Biochem. J. *324*, 529–534.

Ioannou, M.S., Jackson, J., Sheu, S.-H., Chang, C.-L., Weigel, A.V., Liu, H., Pasolli, H.A., Xu, C.S., Pang, S., and Matthies, D. (2019). Neuron-Astrocyte Metabolic Coupling Protects against Activity-Induced Fatty Acid Toxicity. Cell *177*, 1522–1535.

Jasbi, P., Wang, D., Cheng, S.L., Fei, Q., Cui, J.Y., Liu, L., Wei, Y., Raftery, D., and Gu, H. (2019). Breast cancer detection using targeted plasma metabolomics. J. Chromatogr. B Analyt. Technol. Biomed. Life Sci. *1105*, 26–37.

Jha, M.K., and Morrison, B.M. (2018). Glia-neuron energy metabolism in health and diseases: New insights into the role of nervous system metabolic transporters. Exp. Neurol. *309*, 23–31.

Jiang, T., Yin, F., Yao, J., Brinton, R.D., and Cadenas, E. (2013). Lipoic acid restores age-associated impairment of brain energy metabolism through the modulation of Akt/JNK signaling and PGC1α transcriptional pathway. Aging Cell *12*, 1021–1031.

Johnson, E.C.B., Dammer, E.B., Duong, D.M., Ping, L., Zhou, M., Yin, L., Higginbotham, L.A., Guajardo, A., White, B., Troncoso, J.C., et al. (2020). Large-scale proteomic analysis of Alzheimer's disease brain and cerebrospinal fluid reveals early changes in energy metabolism associated with microglia and astrocyte activation. Nat. Med. *26*, 769–780.

Karch, C.M., and Goate, A.M. (2015). Alzheimer's disease risk genes and mechanisms of disease pathogenesis. Biol. Psychiatry *77*, 43–51.

Knoferle, J., Yoon, S.Y., Walker, D., Leung, L., Gillespie, A.K., Tong, L.M., Bien-Ly, N., and Huang, Y. (2014). Apolipoprotein E4 produced in GABAergic interneurons causes learning and memory deficits in mice. J. Neurosci. *34*, 14069–14078.

Li, L.O., Klett, E.L., and Coleman, R.A. (2010). Acyl-CoA synthesis, lipid metabolism and lipotoxicity. Biochim. Biophys. Acta *1801*, 246–251.

Lin, Y.T., Seo, J., Gao, F., Feldman, H.M., Wen, H.L., Penney, J., Cam, H.P., Gjoneska, E., Raja, W.K., Cheng, J., et al. (2018). APOE4 Causes Widespread Molecular and Cellular Alterations Associated with Alzheimer's Disease Phenotypes in Human iPSC-Derived Brain Cell Types. Neuron *98*, 1141–1154.e7.

Liu, C.-C., Liu, C.C., Kanekiyo, T., Xu, H., and Bu, G. (2013). Apolipoprotein E and Alzheimer disease: risk, mechanisms and therapy. Nat. Rev. Neurol. *9*, 106–118.

Liu, L., Zhang, K., Sandoval, H., Yamamoto, S., Jaiswal, M., Sanz, E., Li, Z., Hui, J., Graham, B.H., Quintana, A., and Bellen, H.J. (2015). Glial lipid droplets and ROS induced by mitochondrial defects promote neurodegeneration. Cell *160*, 177–190.

Liu, L., MacKenzie, K.R., Putluri, N., Maletić-Savatić, M., and Bellen, H.J. (2017). The Glia-Neuron Lactate Shuttle and Elevated ROS Promote Lipid Synthesis in Neurons and Lipid Droplet Accumulation in Glia via APOE/D. Cell Metab. *26*, 719–737.e6.

Long, J.M., and Holtzman, D.M. (2019). Alzheimer Disease: An Update on Pathobiology and Treatment Strategies. Cell *179*, 312–339.

Longo, W.E., Grossmann, E.M., Erickson, B., Panesar, N., Mazuski, J.E., and Kaminski, D.L. (1999). The effect of phospholipase A2 inhibitors on proliferation and apoptosis of murine intestinal cells. J. Surg. Res. *84*, 51–56.

Magistretti, P.J., and Allaman, I. (2018). Lactate in the brain: from metabolic end-product to signalling molecule. Nat. Rev. Neurosci. *19*, 235–249.

Mahley, R.W., and Huang, Y. (2012). Apolipoprotein e sets the stage: response to injury triggers neuropathology. Neuron *76*, 871–885.

Marschallinger, J., Iram, T., Zardeneta, M., Lee, S.E., Lehallier, B., Haney, M.S., Pluvinage, J.V., Mathur, V., Hahn, O., Morgens, D.W., et al. (2020). Lipid-droplet-accumulating microglia represent a dysfunctional and proinflammatory state in the aging brain. Nat. Neurosci. *23*, 194–208.

Mauch, D.H., Nägler, K., Schumacher, S., Göritz, C., Müller, E.C., Otto, A., and Pfrieger, F.W. (2001). CNS synaptogenesis promoted by glia-derived cholesterol. Science *294*, 1354–1357.

Nguyen, T.B., Louie, S.M., Daniele, J.R., Tran, Q., Dillin, A., Zoncu, R., Nomura, D.K., and Olzmann, J.A. (2017). DGAT1-Dependent Lipid Droplet Biogenesis

Protects Mitochondrial Function during Starvation-Induced Autophagy. Dev. Cell *42*, 9–21.e5.

Nuriel, T., Angulo, S.L., Khan, U., Ashok, A., Chen, Q., Figueroa, H.Y., Emrani, S., Liu, L., Herman, M., Barrett, G., et al. (2017). Neuronal hyperactivity due to loss of inhibitory tone in APOE4 mice lacking Alzheimer's disease-like pathology. Nat. Commun. *8*, 1464.

Nwabuisi-Heath, E., Rebeck, G.W., Ladu, M.J., and Yu, C. (2014). ApoE4 delays dendritic spine formation during neuron development and accelerates loss of mature spines in vitro. ASN Neuro *6*, e00134.

Olzmann, J.A., and Carvalho, P. (2019). Dynamics and functions of lipid droplets. Nat. Rev. Mol. Cell Biol. *20*, 137–155.

Pellerin, L., and Magistretti, P.J. (1994). Glutamate uptake into astrocytes stimulates aerobic glycolysis: a mechanism coupling neuronal activity to glucose utilization. Proc. Natl. Acad. Sci. USA *91*, 10625–10629.

Peng, J.Y., Lin, C.C., Chen, Y.J., Kao, L.S., Liu, Y.C., Chou, C.C., Huang, Y.H., Chang, F.R., Wu, Y.C., Tsai, Y.S., and Hsu, C.N. (2011). Automatic morphological subtyping reveals new roles of caspases in mitochondrial dynamics. PLoS Comput. Biol. *7*, e1002212.

Posse De Chaves, E.I., Vance, D.E., Campenot, R.B., Kiss, R.S., and Vance, J.E. (2000). Uptake of lipoproteins for axonal growth of sympathetic neurons. J. Biol. Chem. *275*, 19883–19890.

Qi, G., Mi, Y., and Yin, F. (2020). Cellular Specificity and Inter-cellular Coordination in the Brain Bioenergetic System: Implications for Aging and Neurodegeneration. Front. Physiol. *10*, 1531.

Rambold, A.S., Cohen, S., and Lippincott-Schwartz, J. (2015). Fatty acid trafficking in starved cells: regulation by lipid droplet lipolysis, autophagy, and mitochondrial fusion dynamics. Dev. Cell *32*, 678–692.

Rawat, V., Wang, S., Sima, J., Bar, R., Liraz, O., Gundimeda, U., Parekh, T., Chan, J., Johansson, J.O., Tang, C., et al. (2019). ApoE4 Alters ABCA1 Membrane Trafficking in Astrocytes. J. Neurosci. *39*, 9611–9622.

Safieh, M., Korczyn, A.D., and Michaelson, D.M. (2019). ApoE4: an emerging therapeutic target for Alzheimer's disease. BMC Med. *17*, 64.

Schönfeld, P., and Reiser, G. (2017). Brain energy metabolism spurns fatty acids as fuel due to their inherent mitotoxicity and potential capacity to unleash neurodegeneration. Neurochem. Int. *109*, 68–77.

Schulz, J.G., Laranjeira, A., Van Huffel, L., Gärtner, A., Vilain, S., Bastianen, J., Van Veldhoven, P.P., and Dotti, C.G. (2015). Glial β-oxidation regulates Drosophila energy metabolism. Sci. Rep. *5*, 7805.

Shi, Y., Yamada, K., Liddelow, S.A., Smith, S.T., Zhao, L., Luo, W., Tsai, R.M., Spina, S., Grinberg, L.T., Rojas, J.C., et al.; Alzheimer's Disease Neuroimaging Initiative (2017). ApoE4 markedly exacerbates tau-mediated neurodegeneration in a mouse model of tauopathy. Nature *549*, 523–527.

Shimabukuro, M.K., Langhi, L.G., Cordeiro, I., Brito, J.M., Batista, C.M., Mattson, M.P., and Mello Coelho, Vd. (2016). Lipid-laden cells differentially distributed in the aging brain are functionally active and correspond to distinct phenotypes. Sci. Rep. *6*, 23795.

Singh, R., Kaushik, S., Wang, Y., Xiang, Y., Novak, I., Komatsu, M., Tanaka, K., Cuervo, A.M., and Czaja, M.J. (2009). Autophagy regulates lipid metabolism. Nature *458*, 1131–1135.

Smirnova, E., Goldberg, E.B., Makarova, K.S., Lin, L., Brown, W.J., and Jackson, C.L. (2006). ATGL has a key role in lipid droplet/adiposome degradation in mammalian cells. EMBO Rep. *7*, 106–113.

Tambini, M.D., Pera, M., Kanter, E., Yang, H., Guardia-Laguarta, C., Holtzman, D., Sulzer, D., Area-Gomez, E., and Schon, E.A. (2016). ApoE4 upregulates the activity of mitochondria-associated ER membranes. EMBO Rep. *17*, 27–36.

Tracey, T.J., Steyn, F.J., Wolvetang, E.J., and Ngo, S.T. (2018). Neuronal Lipid Metabolism: Multiple Pathways Driving Functional Outcomes in Health and Disease. Front. Mol. Neurosci. *11*, 10.

Xu, P.T., Gilbert, J.R., Qiu, H.L., Ervin, J., Rothrock-Christian, T.R., Hulette, C., and Schmechel, D.E. (1999a). Specific regional transcription of apolipoprotein E in human brain neurons. Am. J. Pathol. *154*, 601–611.

Xu, P.T., Schmechel, D., Qiu, H.L., Herbstreith, M., Rothrock-Christian, T., Eyster, M., Roses, A.D., and Gilbert, J.R. (1999b). Sialylated human apolipoprotein E (apoEs) is preferentially associated with neuron-enriched cultures from APOE transgenic mice. Neurobiol. Dis. *6*, 63–75.

Xu, Q., Bernardo, A., Walker, D., Kanegawa, T., Mahley, R.W., and Huang, Y. (2006). Profile and regulation of apolipoprotein E (ApoE) expression in the CNS in mice with targeting of green fluorescent protein gene to the ApoE locus. J. Neurosci. *26*, 4985–4994.

Yamazaki, Y., Zhao, N., Caulfield, T.R., Liu, C.C., and Bu, G. (2019). Apolipoprotein E and Alzheimer disease: pathobiology and targeting strategies. Nat. Rev. Neurol. *15*, 501–518.

Yao, J., Chen, S., Cadenas, E., and Brinton, R.D. (2011). Estrogen protection against mitochondrial toxin-induced cell death in hippocampal neurons: antagonism by progesterone. Brain Res. *1379*, 2–10.

Yellen, G. (2018). Fueling thought: Management of glycolysis and oxidative phosphorylation in neuronal metabolism. J. Cell Biol. *217*, 2235–2246.

Yin, F., Sancheti, H., and Cadenas, E. (2012). Silencing of nicotinamide nucleotide transhydrogenase impairs cellular redox homeostasis and energy metabolism in PC12 cells. Biochim. Biophys. Acta *1817*, 401–409.

Zechner, R., Strauss, J.G., Haemmerle, G., Lass, A., and Zimmermann, R. (2005). Lipolysis: pathway under construction. Curr. Opin. Lipidol. *16*, 333–340.

Zhao, J., Davis, M.D., Martens, Y.A., Shinohara, M., Graff-Radford, N.R., Younkin, S.G., Wszolek, Z.K., Kanekiyo, T., and Bu, G. (2017a). APOE ε4/ε4 diminishes neurotrophic function of human iPSC-derived astrocytes. Hum. Mol. Genet. *26*, 2690–2700.

Zhao, N., Liu, C.C., Van Ingelgom, A.J., Martens, Y.A., Linares, C., Knight, J.A., Painter, M.M., Sullivan, P.M., and Bu, G. (2017b). Apolipoprotein E4 Impairs Neuronal Insulin Signaling by Trapping Insulin Receptor in the Endosomes. Neuron *96*, 115–129.e5.

Zhu, Y., Nwabuisi-Heath, E., Dumanis, S.B., Tai, L.M., Yu, C., Rebeck, G.W., and LaDu, M.J. (2012). APOE genotype alters glial activation and loss of synaptic markers in mice. Glia *60*, 559–569.

STAR★METHODS

KEY RESOURCES TABLE

REAGENT or RESOURCE	SOURCE	IDENTIFIER
Antibodies		
Rabbit polyclonal to PPAR gamma	Abcam	Cat# ab209350
Rabbit polyclonal to Adipose Triglyceride Lipase (phosphor S406)	Abcam	Cat# ab135093
Total OXPHOS Rodent WB Antibody Cocktail	Abcam	Cat# ab110413; RRID: AB_2629281
Rabbit polyclonal to PGC1 alpha + beta	Abcam	Cat# ab72230; RRID: AB_1640773
ApoE (pan) (D719N) Rabbit mAb	Cell Signaling Technology	Cat# 13366; RRID: AB_2798191
Akt (pan) (C67E7) Rabbit mAb	Cell Signaling Technology	Cat# 4691S; RRID: AB_915783
Phospho-Akt (Ser473) (D9E) XP Rabbit mAb	Cell Signaling Technology	Cat# 4060S; RRID: AB_2315049
OPA1 (D6U6N) Rabbit mAb	Cell Signaling Technology	Cat# 80471; RRID: AB_2734117
DRP1 (D6C7) Rabbit mAb	Cell Signaling Technology	Cat# 8570; RRID: AB_10950498
SREBP-1 (2A4): sc-13551	Santa Cruz Biotechnology	Cat# sc-13551; RRID: AB_628282
SNAP25 (D7B4) Rabbit mAb	Cell Signaling Technology	Cat# 5308; RRID: AB_10621948
PSD95 (D74D3) Rabbit mAb	Cell Signaling Technology	Cat# 3409; RRID: AB_1264242
Hexokinase I (C35C4) Rabbit mAb	Cell Signaling Technology	Cat# 2024; RRID: AB_2116996
Hexokinase II (C64G5) Rabbit mAb	Cell Signaling Technology	Cat# 2867; RRID: AB_2232946
Glial fibrillary acidic protein antibody	MED Millipore	Cat# MAB360; RRID: AB_11212597
TOMM20 antibody	Abcam	Cat# ab186734; RRID: AB_2716623
Monoclonal Anti-MAP2 antibody	Sigma	Cat# M4403; RRID: AB_477193
Perilipin-2/ADFP antibody	Novus Biologicals	Cat# NB110-40877; RRID: AB_787904
ApoE4 antibody	Novus Biologicals	Cat# NBP1-49529; RRID: AB_10011579
Phospho-AMPKα (Thr172)(40H9) Rabbit mAb	Cell Signaling Technology	Cat# 2535; RRID: AB_331250
AMPKα (D63G4) Rabbit mAb	Cell Signaling Technology	Cat# 5832; RRID: AB_10624867
Acetyl-CoA Carboxylase Antibody	Cell Signaling Technology	Cat# 3662; RRID: AB_2219400
Phospho-Acetyl-CoA Carboxylase (Ser79) Antibody	Cell Signaling Technology	Cat# 3661; RRID: AB_330337
β-actin (8H10D10) Mouse mAb	Cell Signaling Technology	Cat# 3700; RRID: AB_2242334
Fatty Acid Synthase (C20G5) Rabbit mAb	Cell Signaling Technology	Cat# 3180; RRID: AB_2100796
Mouse Anti-PDH-E1α Antibody	Mitoscience	Cat# MSP07; RRID: AB_478296
PhosphoDetect Anti-PDH-E1α ($pSer^{293}$) Rabbit pAb	Sigma	Cat# AP1062; RRID: AB_10616069
Goat anti-rabbit IgG (H+L)	Vector Laboratories	Cat# PI-1000; RRID: AB_2336198
Goat anti-mouse IgG (H+L)	Vector Laboratories	Cat# PI-2000; RRID: AB_2336177
Alexa Fluor 488 goat anti-mouse	Thermo Fisher Scientific	Cat# A11001; RRID: AB_2534069
Alexa Fluor 488 goat anti-rabbit	Thermo Fisher Scientific	Cat# A11008; RRID: AB_143165
Alexa Fluor 555 goat anti-mouse	Thermo Fisher Scientific	Cat# A21422; RRID: AB_2535844
Chemicals, Peptides, and Recombinant Proteins		
BODIPY FL C16	Thermo Fisher Scientific	Cat# D3821
BODIPY 558/568 C12	Thermo Fisher Scientific	Cat# D3835
BODIPY 581/591 C11	Thermo Fisher Scientific	Cat# D3861
HCS LipidTOX™ Green Neutral Lipid Stain	Thermo Fisher Scientific	Cat# H34475
HCS LipidTOX™ Red Neutral Lipid Stain	Thermo Fisher Scientific	Cat# H34476
DMEM/F-12, HEPES, no phenol red	Thermo Fisher Scientific	Cat# 11039047
HBSS, no calcium, no magnesium	Thermo Fisher Scientific	Cat# 14170112
DPBS	Thermo Fisher Scientific	Cat# 14287080
B-27 Plus Neuronal Culture System	Thermo Fisher Scientific	Cat# A3653401
Fetal Bovine Serum	ATCC	Cat# 302020

(*Continued on next page*)

Continued

REAGENT or RESOURCE	SOURCE	IDENTIFIER
3-methyladenine (3-MA)	Sigma	Cat# M9281-100MG
XF Palmitate-BSA FAO Substrate	Agilent	Cat# 102720-100
MitoTracker Green FM	Thermo Fisher Scientific	Cat# M7514
ND-630	Bio Vision	Cat# B2248-5
Triacsin C	Cayman Chemical	Cat# 10007448500
Atglistatin	Cayman Chemical	Cat# 1469924-27-3
Pitstop 2	Sigma	Cat# SML1169
Adenosine 5′-diphosphate sodium salt	Sigma	Cat# A2754-1G
TaqManFast Advanced Master Mix	Thermo Fisher Scientific	Cat# 4444557
RTA Midi PVDF Transfer Kit	Bio-Rad	Cat# 1704273
4–15% Criterion TGX Precast MidProtein Gel	Bio-Rad	Cat# 5671085
Oligomycin A	Sigma	Cat# 75351-5MG
Methyl arachidonyl fluorophosphonate (MAFP)	Cayman Chemical	Cat# 706601010MG
Recombinant Human ApoE3	Fitzgerald Industries	Cat# 30R-2381
Recombinant Human ApoE4	Fitzgerald Industries	Cat# 30R-2382
Critical Commercial Assays		
Seahorse XF Mito Fuel Flex Test Kit	Agilent	Cat# 103260-100
Lactate Colorimetric/Fluorometric Assay Kit	Bio Vision	Cat# K607-100
Triglyceride Quantification Colorimetric/Fluorometric Kit	Bio Vision	Cat# K622-100
Free Fatty Acid Fluorometric Assay Kit	Cayman Chemical	Cat# 700310-96
Glucose Uptake Cell-Based Assay Kit	Cayman Chemical	Cat# 600470
Adult Brain Dissociation Kit	Miltenyi Biotec	Cat# 130-107-677
ATP Determination Kit	Thermo Fisher Scientific	Cat# A22066
Low Density Lipoprotein Uptake Kit	Thermo Fisher Scientific	Cat# I34359
Lipid Extraction Kit (Chloroform Free)	Abcam	Cat# ab211044
Lipid Assay Kit (unsaturated fatty acids)	Abcam	Cat# ab242305
Experimental Models: Organisms/Strains		
Mouse: B6(SJL) -$^{Apoeem2(ApoE*)Adiuj}$/J	The Jackson Laboratory	Stock No: 029018
Mouse: B6(SJL)-$^{Apoetm1.1(ApoE*4)Adiuj}$/J	The Jackson Laboratory	Stock No: 027894
Mouse: C57BL/6J	The Jackson Laboratory	Stock No: 000664
Oligonucleotides		
APOE (Hs00171168_m1)	Life Technologies	Cat# 4331182
Actb (Mm00607939_s1)	Life Technologies	Cat# 4331182
Software and Algorithms		
GraphPad Prism 9	GraphPad Software	https://www.graphpad.com/
Imaris 9.3.0	Oxford Instruments	https://imaris.oxinst.com/
Image Lab 6.0.1	Bio-Rad	https://www.bio-rad.com/
MetaboAnalyst 4.0	Chong et al., 2019	https://www.metaboanalyst.ca
BioRender	BioRender	https://biorender.com
Micro-P Software	Peng et al., 2011	N/A

RESOURCE AVAILABILITY

Lead Contact

Further information and requests for resources should be directed to and will be fulfilled by the Lead Contact, Fei Yin (feiyin@arizona.edu).

Materials Availability

This study did not generate any unique reagents.

Data and Code Availability

All used software is listed in the Key Resources Table. This study did not generate any unique datasets or new code.

EXPERIMENTAL MODEL AND SUBJECT DETAILS

All animal experiments were approved by the University of Arizona Institutional Animal Care and Use Committee (IACUC). Humanized ApoE3 (029018) and ApoE4 (027894) knockin mice (homozygous) and the wild-type C57BL/6J mice were obtained from the Jackson Laboratory and bred at the University of Arizona animal facility. All mice were housed in a temperature (23°C) and humidity-controlled room with a 12-h light and 12-h dark cycle with *ad libitum* access to water and standard laboratory global 2019 diet (23% calories from protein, 22% calories from fat, 55% calories from carbohydrate, 3.3 kcal/g; Envigo) and cared in facilities operated by University Animal Care. 3-month male mice were used for primary astrocyte isolation and *in vivo* / *ex vivo* assays. Timed pregnant mice of designated genotype were prepared for the isolation of E17 embryonic hippocampal neurons.

METHOD DETAILS

Isolation and culture of primary hippocampal neurons

Primary embryonic hippocampal neurons from humanized ApoE3 or ApoE4 mice were prepared as previously described (Yao et al., 2011). Briefly, hippocampi were dissected from the brains of embryonic day 17 fetuses. Hippocampal tissues were dissociated by incubation with 0.02% trypsin in HBSS (5.4 mM KCl, 137 mM NaCl, 0.4 mM KH_2PO_4, 0.34 mM $Na_2HPO_4 \cdot 7H_2O$, 10 mM glucose, and 10mM HEPES) for 3 min at 37°C and repeated passage through a series of fire-polished constricted Pasteur pipettes. Cell suspension was filtered through 40 μm Nylon cell strainer into 50 mL conical centrifuge tubes and centrifuged at 1,000 rpm for 3min. The purity of cultured neurons was > 94% while GFAP-positive cells are < 1% as determined by NeuN, GFAP and DAPI immunostaining on DIV8. For imaging or immunocytochemistry studies, 20,000 cells were plated onto each poly-D-lysine (50 μg/mL) coated 22-mm coverslips. For immunoblotting, 10^6 cells were seeded on 50 μg/mL poly-D-lysine coated 6 well plates. For Extracellular Flux (Seahorse) analyses, 50,000 or 25,000 cells were plated onto each well of the 24-well, or 96-well XF microplates, respectively. Neurons were grown in Neurobasal Plus Medium supplemented with 25 μM glutamate, 500 μM glutamine, 0.1% penicillin/streptomycin, and 2% B27 Plus supplement at 37°C in a humidified 5% CO_2 atmosphere. Experiments were performed after 7 days in culture unless otherwise specified.

Isolation and culture of primary astrocytes

Primary astrocytes were isolated using an Adult Brain Dissociation Kit (Cat# 130-107-677, Miltenyi Biotech) as described in Batiuk et al. (2017) with slight modifications. Fresh mouse brain tissue (excluding cerebellum and brain stem) was enzymatically digested followed by mechanical dissociation with the gentleMACS Dissociator with Heaters. After dissociation, myelin and cell debris were removed using the Debris Removal Solution and erythrocytes removed by the Red Blood Cell Removal Solution. The Anti-ACSA-2 MicroBeads was used to isolate astrocytes from the single-cell suspension. Microglia are removed by overnight shaking in the incubator and the remaining astrocytes are verified for negative microglia staining (Iba1) before experimental use. Isolated astrocytes were cultivated in DMEM/F12 with 10% FBS and 0.2% penicillin/streptomycin for two weeks before use.

Co-culture of primary neurons with astrocytes

48 hours before neuron isolation, isolated astrocytes were plated in poly-D-lysine coated, 24 well or 6 well 0.4 μm cell-culture inserts at a density of 50,000 or $1x10^6$ cells/well, respectively. 1 hour after isolated neurons were adhered to plates, astrocyte inserts were replaced with neuronal medium and placed into wells with neuronal cultures. Neuron-astrocyte co-cultures were maintained at 37°C with 5% CO_2 for various times before different treatment, after which plates with neurons and inserts with astrocytes were separated for various analyses.

Neuronal culture with astrocyte conditioned medium (ACM)

Astrocyte conditioned medium (ACM) was collected from cultures of adult ApoE3 or ApoE4 astrocytes and passed through a 0.2 μm filter. DIV8 neurons were washed with warm PBS and incubated with 70% neuronal medium (as described in the neuron culture section) and 30% ACM at 37°C with 5% CO_2 for 48 h.

Immunostaining and confocal imaging

Cells cultured on coverslips were fixed with 4% paraformaldehyde for 15 minutes, rinsed with PBS for 3 times and incubated in blocking buffer (5% normal goat serum + 0.3% Triton X-100 in PBS) for 1 h at room temperature. Anti-MAP-2 (1:1000, Sigma, M4403) or anti-Perilipin-2 (1:200, Novus, NB110-40877) primary antibody (diluted in blocking buffer) staining was performed overnight at 4°C. Secondary antibody (Alexa Fluor 488 goat anti-mouse, 1:1000, Invitrogen or Alexa Fluor 488 goat anti-rabbit, 1:1000, Invitrogen) staining was conducted at room temperature for 1 h. Coverslips were mounted with mounting medium containing DAPA on slides and sealed with nail polish after cleaning the edge. Images were captured with Zeiss Laser-Scanning Microscopy (LSM) 880 with

Airyscan detector using 40x water objective lens or 63x oil objective lens. Quantification of neurite length, branch, and area was performed using Imaris 9.3.0 software. Each data point represents the averaged value of all cells on a coverslip.

Lipid droplets staining and quantification

Lipid droplets in neurons and astrocytes were stained by HCS LipidTOX Red Neutral Lipid Stain following the manufacturer's instruction. Cells were washed by PBS and pretreated with or without the following inhibitors: 3-MA (5 mM), ND-630 (10 nM), Triacsin C (2.5 μM), BFA (5 μg/mL), MAFP (0.5 μM), Compound C (5 μM), AICAR (0.5 mM), Atglistatin (0.5 μM), in Neurobasal Plus Medium or DMEM/F12 medium containing 0.2% penicillin/streptomycin for 12 h at 37°C. After medium was removed, cells were rinsed with PBS for 3 times, fixed in 4% Paraformaldehyde (PFA) for 30 minutes and stained with 1X LipidTOX for 30 minutes at room temperature. Z section images were captured with Zeiss LSM 880 with Airyscan and three-dimensional images were generated. The number and volume of lipid droplets were quantified by the surface module of Imaris 9.3.0 from at least 3 animals or batches of cell cultures; n = 3-8 coverslips/condition; 8 ± 2 cells/coverslip. Each data point represents the averaged value of all cells on a coverslip.

RNA extraction and RT-qPCR

Total RNA was isolated from neurons or astrocytes using PureLink RNA Mini Kit (Cat# 12183018A, Thermo Fisher). RNA quantity and RNA quality were evaluated by NanoDrop One Microvolume UV-Vis Spectrophotometer (Thermo Fisher). Extracted RNA was reverse transcribed to cDNA using the SuperScript IV VILO Master Mix with ezDNase Enzyme kit (Cat# 11766050, Thermo Fisher). TaqMan probes (Mm00607939_s1 for β-actin and Hs00171168_m1 for ApoE) and the TaqMan Fast Advanced Master Mix kit (Cat# 4444557, Thermo Fisher) were used for qPCR using QuantStudio 6 Real-Time PCR Systems (Thermo Fisher). Relative ApoE gene expression levels to the reference group were calculated by the comparative Ct (ΔΔCt) method, with Ct denoting threshold cycle. ΔCt was calculated as the difference in average Ct of the ApoE and Actb, and $2^{-\Delta Ct}$ was normalized to $2^{-\Delta Ct}$ of the reference group.

Cellular glucose uptake assay

2.5×10^4 cells/well were plated in 96-well plates, washed twice, and incubated with 100 μM 2-NBDG (BioGems) for 30 minutes. Cells cultured in the absence of 2-NBDG served as a control. Incubated cells were washed twice, and the fluorescence intensity was quantified using Cytation 5 Cell Imaging Multi-Mode Reader (BioTek) with Ex/Em = 465/540 nm.

Mitochondrial membrane potential

Relative mitochondrial membrane potential was determined by MITO-ID® Membrane potential detection kit (Enzo Life Sciences) using a cationic dye that fluoresces either green or orange depending upon membrane potential status. 2.5×10^4 cells/well in a 96-well plate were washed with a 1 × Mito-ID assay solution and stained with Mito-ID dye for 15 min at room temperature in the dark, and fluorescently analyzed by Cytation 5 Imaging Multi-Mode Reader. Orange and green fluorescence intensity was measured separately at Ex/Em = 540/570 nm and 480/530 nm, respectively, and the ratio of orange/green intensity was calculated and normalized to control group.

LDL uptake assay

LDL uptake assay in astrocytes was conducted using the BODIPY FL LDL uptake kit (Thermo Fisher Scientific) following manufacturer's instructions. 5×10^4 cells/well in 96-well plates were replaced with serum starved medium (DMEM plus 0.3% BSA) for 12 h. After starvation, cells were incubated with 6 μg/mL BODIPY FL LDL for 3 h at 37 °C and after washing, fluorescent density was determined by Cytation 5 Imaging Multi-Mode Reader with excitation at Ex/Em = 540/570 nm.

Lipid peroxidation assay

Lipid peroxidation assay were performed using BODIPY 581/591 C11 (Lipid Peroxidation Sensor). DIV8 neurons grown on PDL-coated 96 well plate were washed with warm HBSS and incubated with 2 μM BODIPY 581/591 C11 at 37°C with 5% CO_2 for 1 h. Fluorescence intensities were measured at Ex/Em = 500/510 nm and 581/591 nm by Cytation 5 Cell Imaging Multi-Mode Reader (BioTek), and the ratio of the fluorescence intensities at 510 nm to 591 nm was calculated and normalized to control group.

ApoE levels in culture medium

ApoE levels in culture medium were measured with the Human ApoE (AD2) ELISA Kit (Thermo Scientific) following manufacturer's instructions. Incubated plates were read with Cytation 5 Cell Imaging Multi-Mode Reader at 450 nm and 550 nm for absorbance. Values at 550 nm were subtracted from 450 nm values to correct for optical imperfections in the microplate.

Lactate levels

Lactate levels in medium or cell lysate were measured by the Lactate Colorimetric/Fluorometric Assay Kit (BioVision) following manufacturer's instructions. Cell lysate or medium was incubated with Reaction Mix for 30 minutes at room temperature in the dark and fluorescence was determined at Ex/Em = 535/587 nm.

Total triacylglycerol

Total triacylglycerol levels were determined using triglyceride quantification kit (Bio Vision) following manufacturer's instructions. 1×10^6 cells were collected and centrifuged at 1000 x g for 10 minutes at 4°C. Cell pellet was resuspended in 1 mL solution containing 5% NP-40 in water and sonicated, slowly heated to 80-100°C in a water bath for 5 min and cooled down to room temperature. Cell suspensions were centrifuged at 15,000 rpm for 10 minutes at 4°C. Supernatant was collected on ice and processed for quantification. Relative fluorescence intensities were measured at Ex/Em = 535/590 nm.

Total free fatty acids

Total free fatty acid levels in neurons or astrocytes were determined using Free Fatty Acid Quantification Assay Kit (Abcam). 1×10^6 cells were collected and centrifuged at 1000 g for 10 minutes at 4°C. Cell pellet was homogenized in 200 μL Triton X-100 (1% Triton X-100 in chloroform) using a micro-homogenizer, and centrifuged at 15000 rpm for 10 minutes at 4°C. The organic phase (lower phase) was collected, air-dried at 50°C in a fume hood followed by vacuum dry for 30 minutes to remove chloroform. Dried lipids were dissolved in 200 μL of Fatty Acid Assay Buffer by vortexing extensively for 5 minutes and processed for quantification. Fatty acid levels were fluorescently measured at Ex/Em = 535/587 nm.

Unsaturated fatty acids

Total unsaturated fatty acid levels in neurons were prepared by lipid extraction Kit (Abcam) and measured by Lipid Assay Kit for unsaturated fatty acids (Abcam) following the manufacturer's instructions. 1×10^6 neurons were collected in 1.5 mL micro centrifuge tube and centrifuged at 1000 x g for 5 minutes. Cell pellets were washed and resuspended in 25 μL PBS, and 500 μL extraction buffer was added. After agitating the mixture for 15-20 minutes at room temperature, sample tubes were centrifuged at 10,000 x g for 5 minutes. The supernatant was carefully collected and dried in a 37°C incubator overnight. Dried lipid extract was resuspended in 50 μL suspension buffer and sonicated for 15-20 minutes at 37°C before quantification. Absorbance was measured at OD 540 nm.

ATP levels

The levels of cellular ATP were measured by ATP determination kit (Eugene) following the manufacturer's instructions. Cells cultured in 96-well plate at a density of 2.5×10^4 cells/well were incubated with 1.25 μg/mL of firefly luciferase, 50 μM D-luciferin and 1 mM DTT in 100 μL 1 x Reaction Buffer. After 15 minutes of incubation, luminescence (emission maximum ~560 nm) was measured by Cytation 5 Cell Imaging Multi-Mode Reader.

Mitochondrial flux assay

Metabolic flux analysis was performed as described previously (Jiang et al., 2013; Yin et al., 2012). A schematic diagram of a typical Seahorse Mito Stress Test was shown in Figure S2B. Primary neurons or astrocytes were cultured on poly-D-lysine coated Seahorse 24- or 96-well plates at a density of 50,000 or 25,000 cells per well, respectively. Neurons were grown in Neurobasal Plus Medium + B27 Plus supplement for one week prior to experiment. Astrocytes were grown in DMEM/F12 medium containing 10% FBS. On the day of analysis, culture medium was replaced with unbuffered DMEM (DMEM base medium supplemented with 25 mM glucose, 1 mM sodium pyruvate, 31 mM NaCl, 2 mM glutamine; pH 7.4) and incubated at 37°C in a CO_2-free incubator for 1 h. All medium and injection reagents were adjusted to pH 7.4 on the day of assay. Three baseline measurements of OCR (oxygen consumption rate) and ECAR (extracellular acidification rate) were sampled prior to sequential injection of mitochondrial inhibitors: oligomycin A (ATP synthase complex V inhibitor) at 4 μM), FCCP (an uncoupling agent that collapses the proton gradient and disrupts the mitochondrial membrane potential, which can induce freely flow of electron through the ETC and maximal oxygen consumption by complex IV) at 1 μM, and rotenone/antimycin A (complex I inhibitor and III inhibitors, which in combination shut down mitochondrial respiration) at 1 μM / 1 μM. OCR and ECAR were recorded by the Seahorse XFe24 or XFe96 instrument and normalized to the total protein concentration in each well. The basal respiration was calculated as the differences between OCR before oligomycin injection and OCR after rotenone/antimycin A injection (non-mitochondrial respiration). Maximal respiration was the differences between maximal OCR value after FCCP injection and OCR after rotenone/antimycin A injection. Spare capacity ratio (SCR) is defined as the ratio of maximal respiration to basal respiration, as an indicator for the utilization of the cells' maximum bioenergetic capacity. Experiments from cells isolated from at least three animals were performed in these assays. For each animal or cell batch, there were 6-8 wells/group and 50,000 cells/well for 24-well platform, and 16-20 well/group and 25,000 cells/well for 96-well platform. Data shown are representative result from at least 3 independent batches/animals of cells.

Mitochondrial FA metabolic test

Mitochondrial FA oxidation test was conducted following user manual of Agilent Seahorse XF Palmitate Oxidation Stress Test Kit (Cat#: 102720-100). Cells were prepared as described in the mitochondrial flux assay above. DMEM/F12 growth medium from 96-well culture plates was replaced with substrate-limited medium (DMEM base medium supplemented with 0.5 mM glucose, 1.0 mM glutMAX, 0.5 mM carnitine, and 1% FBS, pH 7.4) and incubate for 12 hours prior to the assay to eliminate endogenous substrates. On the day of analysis, cell medium was replaced with FAO assay buffer (111 mM NaCl, 4.7 mM KCl, 1.25 mM $CaCl_2$, 2.0 mM $MgSO_4$, 1.2 mM NaH_2PO_4) and incubated at 37°C in a CO_2-free incubator for 1 h. Then BSA control or Palmitate:BSA were added to each wells prior to the initiation of XF assay. The following steps were performed as described in the mitochondrial flux assay above.

Mitochondrial fuel flex test

Mitochondrial fuel flex test was performed to determine relative dependency and capacity of astrocytes on different metabolic fuels. Assay was conducted following user manual of XF Mito Fuel Flex Test Kit (Cat#: 103260-100, Agilent). Astrocytes were prepared as described in the XF flux assay above, and three baseline measurements of OCR (Oxygen Consumption Rate) were sampled prior to the injection of combination of fuel pathway inhibitors (UK5099, mitochondrial pyruvate carrier inhibitor that inhibits glucose oxidation pathway; BPTES, glutaminase Inhibitor that inhibits glutamine oxidation pathway; or Etomoxir, CPT1 inhibitor that inhibits long-chain fatty acid oxidation). Sequentially inhibiting the pathway of interest followed by the inhibition of two alternative pathways enables the calculation of the dependency of cells on the pathway of interest for their basal energy demand. For each pathway, fuel dependency was calculated by:

$$Dependency\ (\%) = \frac{Basal\ OCR - OCR\ after\ inhibition\ of\ target\ pathway}{Basal\ OCR - OCR\ after\ inhibition\ of\ all\ pathways} \times 100$$

Sequentially inhibiting the two alternative pathways followed by the inhibition of the pathway of interest enables the calculation of the capacity of cells utilizing the pathway of interest for their basal energy demand. For each pathway, fuel capacity was calculated by:

$$Dependency\ (\%) = \frac{Basal\ OCR - OCR\ after\ inhibition\ of\ alternate\ pathways}{Basal\ OCR - OCR\ after\ inhibition\ of\ all\ pathways} \times 100$$

The difference between fuel capacity and dependency was calculated as the flexibility of each fuel pathway.

Acute brain slice metabolic analysis

Acute brain slice respiration assay was performed by adapting previously developed procedure (Fried et al., 2014) with modifications to include free FAs as substrates in addition to glucose. 3-month male ApoE3 and ApoE4 knockin mice were decapitated after isoflurane anesthesia and the brain was rapidly removed and immersed in artificial cerebrospinal fluid (aCSF) with 0 mM glucose at 0-4°C containing: 120 mM NaCl, 3.5 mM KCl, 1.3 mM $CaCl_2$, 1 mM $MgCl_2$ hexahydrate, 0.4 mM KH_2PO_4, 5 mM HEPES,10 mM sucrose, and 4 mg/mL BSA. The brain (excluding cerebellum and brain stem) was pasted to the slicing cutter with adhesive and cut it to contain the hippocampus and coronal 250 μm thick slices at 4°C. After sectioning, 1-mm stainless steel biopsy punches (Miltex, York, PA) was used to prepare circular sections (1 mm diameter) of tissues which were then transferred into XF Islet Capture Microplate (101174-100; Agilent, Billerica, MA). Brain slices were incubated with glucose-containing aCSF (10 mM glucose) or aglycemic aCSF (10 mM sucrose) at 37°C in CO_2-free incubator for 1 h. Four baseline measurements of OCR and ECAR were sampled, followed by sequential injection of: BSA control of BSA-Oleate (150 μM), oligomycin A (2 μg/mL), FCCP (1 μM), and antimycin A (2 μM) (all are final concentrations in well). OCR and ECAR were recorded by the Seahorse XFe24 as described in the above section for cell cultures.

Immunoblotting and quantification

Protein concentrations of cell lysate of neurons and astrocytes were determined by Protein Assay Dye Reagent (Bio-Rad). Equal amounts of proteins (10-20 μg) were loaded and separated on a 4%–15% Criterion Precast Midi Protein Gel (Bio-Rad) and then transferred to a 0.45 μm pore size polyvinylidene difluoride (PVDF) membrane and immunoblotted with the appropriate primary antibodies. Primary antibodies were incubated overnight, followed by washing and probing with the appropriate HRP-conjugated anti-rabbit or anti-mouse secondary antibody (Vector Laboratories, Burlingame, CA). The immunoreactive bands were visualized by Pierce SuperSignal Chemiluminescent Substrate or SuperSignal West Femto Maximum Sensitivity Substrate (Thermo Scientific, IL) and captured by ChemiDoc Imaging System (BioRad, Hercules, CA). Saturated pixel highlighting feature of the instrument was used to prevent image overexposure for chemiluminescence. Band intensity was quantified using Image Lab 6.0.1 (Bio-Rad, Hercules, CA).

Inter-cellular fatty acid transfer (pulse-chase) assay

DIV7 ApoE3 or ApoE4 neurons or adult astrocytes (0.5×10^6 cells/well in 6-well plate) were incubated with 2 μM BODIPY 558/568 C12 in Neurobasal Plus Medium containing 2% B27 Plus for 16 h and then washed with PBS for three times. These labeled cells (donor) were then transferred to co-culture with previously prepared unlabeled astrocytes or neurons (recipient, 100,000 cells on 22 mm coverslip) for 4 h. Recipient cells on coverslips were then washed with PBS and fixed. Fluorescent images were captured by Cytation 5 Imaging Multi-Mode Reader and analyzed to quantify positively labeled recipient cells using ImageJ 1.8.0.

Transmission electron microscope (TEM) analysis

Primary neurons or astrocytes were fixed *in situ* in 6-well plate with 2.5% glutaraldehyde in 0.1 M Pipes buffer for 30 minutes, washed with 0.1 M Pipes/glycine for 10 minutes and post-fixed with 1% osmium tetroxide in deionized water (DIW). Following a further wash in DIW, cells were carefully scraped off cell bottoms, transferred to microfuge tubes and pelleted. Pellets were stained with 2% uranyl acetate, dehydrated through an alcohol-acetonitrile series and infiltrated with acetonitrile/Spurr's resin overnight. Following further infiltration with 100% resin blocks were allowed to polymerize at 60°C overnight. Blocks were removed from the microfuge tubes and 70 nm sections cut on an RMC PTXL ultramicrotome onto uncoated 150 mesh copper grids and stained with 2% lead citrate for

2 minutes. Sections were viewed in a Tecnai T12 electron microscope operated at 100 kV. 8-bit Tiff images were captured on an AMT XR41 CCD camera for analysis.

Mitochondrial morphological subtype analysis

Adult astrocytes were stained with MitoTracker (Invitrogen) and cell images were captured by Zeiss LSM 880 with Airyscan. Quantification of images were then performed using Micro-P software (Peng et al., 2011). Individual mitochondria were categorized based on their area, morphology, and length into six distinct subtypes: small globules, swollen globules, straight tubules, twisted tubules, branched tubules and loops. The quantity of fused mitochondria (fusion products) was calculated by combining the number of straight tubule-, twisting tubule-, loop- and branch tubule mitochondrial populations. The numbers of small globule and swollen globule mitochondria were combined and classified as fragmented mitochondria (fission products). High-powered (400 x) fields of micrographs from three independent experiments per group were analyzed.

Fatty acid mass spectrometry (MS) analysis

After culture medium collection, cells in 6-well plates were rinsed with 2 mL of 37°C PBS for 1 time and 1 mL of −75°C 8:2 methanol: H_2O was immediately added into each well on dry ice and incubated for 30 minutes. Cells were then scraped from culture wells at −75°C and transferred to 1.7 mL tubes. 0.7 mL 8:2 methanol: H_2O was added to the culture wells to perform further extraction. Two extractions were combined and centrifuged at 13,000 rpm for 5 minutes at 4°C. Soluble extract was transferred to another tube and completely dried using the Speedvac vacuum at 30°C. Protein concentration of the pellets was measured and used for MS loading normalization. Prior to MS analysis, the obtained residue was reconstituted in 150 μL 40% PBS/60% ACN. A quality control (QC) sample was pooled from all the study samples.

Targeted LC-MS/MS was performed as described previously (Gu et al., 2015; Jasbi et al., 2019). Briefly, all LC-MS/MS experiments were performed on an Agilent 1290 UPLC-6490 QQQ-MS (Santa Clara, CA) system. Each sample was injected twice, 10 μL for analysis using negative ionization mode and 4 μL for analysis using positive ionization mode. Both chromatographic separations were performed in hydrophilic interaction chromatography (HILIC) mode on a Waters XBridge BEH Amide column (150 × 2.1 mm, 2.5 μm particle size, Waters Corporation, Milford, MA). The flow rate was 0.3 mL/min, auto-sampler temperature was kept at 4°C, and the column compartment was set at 40°C. The mobile phase was composed of Solvents A (10 mM ammonium acetate, 10 mM ammonium hydroxide in 95% H_2O/5% ACN) and B (10 mM ammonium acetate, 10 mM ammonium hydroxide in 95% ACN/5% H_2O). After the initial 1-minute isocratic elution of 90% B, the percentage of Solvent B decreased to 40% at t = 11 min. The composition of Solvent B maintained at 40% for 4 min (t = 15 min), and then the percentage of B gradually went back to 90%, to prepare for the next injection. The mass spectrometer is equipped with an electrospray ionization (ESI) source. Targeted data acquisition was performed in multiple-reaction-monitoring (MRM) mode. The whole LC-MS system was controlled by Agilent Masshunter Workstation software (Santa Clara, CA). The extracted MRM peaks were integrated using Agilent MassHunter Quantitative Data Analysis (Santa Clara, CA). Metabolomics data are processed and heatmaps generated using MetaboAnalyst 4.0 (Chong et al., 2019).

QUANTIFICATION AND STATISTICAL ANALYSIS

Statistical analysis was performed using Graphpad Prism 7.0. Statistical significance was determined by two-tailed Student's t test for paired comparisons and one-way ANOVA with post hoc Turkey test for multiple comparisons. Data were presented as the means ± SEM from at least three independent experiments. The exact number of technical and experimental replicates can be found in the figure legends for each experiment. * $p < 0.05$, ** $p < 0.01$.